The Ohio Valley Wave-Merger Cyclogenesis Event of 25–26 January 1978. Part II: Diagnosis Using Quasigeostrophic Potential Vorticity Inversion

GREGORY J. HAKIM, DANIEL KEYSER, AND LANCE F. BOSART

Department of Atmospheric Science, State University of New York at Albany, Albany, New York

ABSTRACT

The dynamical interactions between precursor disturbances during the wave-merger cyclogenesis event of 25–26 January 1978 over eastern North America are diagnosed using quasigeostrophic potential vorticity (QGPV) inversion. This case is characterized by two prominent preexisting upper-level disturbances that induce rapid surface cyclogenesis as they come into close proximity. Static QGPV inversion is used to attribute a particular geopotential height field to the QGPV associated with each precursor disturbance. The full flow is partitioned into the following components: the northern upper precursor, the southern upper precursor, and the background flow. Prognostic QGPV inversion is used to quantify the instantaneous geopotential height tendencies attributable to each of these flow components.

The static-inversion results for the upper precursors exhibit the structure of baroclinic vortices with maximum amplitude near the tropopause. During the 48-h period spanning the period of study of this event, these vortices rotate cyclonically about a point between them with the rate of rotation increasing as the vortices draw closer together. The background flow appears as a synoptic-scale trough, with the meridional tilt of the trough axis positive (negative) prior to (during) rapid surface cyclogenesis. Prior to surface cyclogenesis, the background flow is also confluent in the vicinity of the vortices, acting to bring them closer together. Rapid surface cyclogenesis occurs as the vortices achieve their closest approach (i.e., "merge"). Three interaction signatures are identified and quantified with prognostic QGPV inversion: vortex–vortex (vortex-induced flows advecting the QGPV of other vortices), vortex-retrogression (vortex-induced flows advecting background QGPV), and background-flow advection of vortex QGPV. Solutions for the observed case confirm that the vortex–vortex interactions become more robust as the vortices come closer together. However, the background advections are dominant and act to bring the vortices closer together. Nearly all of the geopotential height falls at the 1000-hPa cyclone center are due to the advection of the upper precursors by the background flow during the entire cyclogenesis event.

A simple model is proposed that includes the three primary elements of this case: two vortices and a background flow. For a barotropic atmosphere on an f plane, the vortices are represented by rigid vortex patches and the background flow by a hyperbolic deformation field that is fixed in time. Solutions representative of observed parameters exhibit many of the properties of the observed case, including "merger." Solutions corresponding to merger are found to be extremely sensitive to small changes in the deformation field for a given set of initial conditions describing vortex position, size, and strength, suggesting limitations to the predictability of the merger phenomenon.

1. Introduction

The problem of extratropical cyclogenesis has been approached by both analysis of observations and development of theory. The current observational paradigm describes interactions between upper- and lower-level disturbances, which often achieve large amplitude prior to interaction. Traditionally, theory has emphasized the stability of basic states and has been less concerned with the initial structure of disturbances. Recently, better agreement with observations has been demonstrated by consideration of the initial-value problem (Farrell 1984, 1985, 1989) and analysis of cyclone evolution in terms of interactions between upper- and lower-level disturbances (e.g., Hoskins et al. 1985, hereafter HMR; Rotunno and Fantini 1989; Whitaker and Barcilon 1992; Davies and Bishop 1994). These descriptions of development focus on a single upper-level disturbance. There are observations indicating that certain cyclogenesis events occur in the presence of more than one upper-level disturbance, such as wave-merger cyclogenesis (Lai and Bosart 1988; Gaza and Bosart 1990). These events involve not only vertical interactions but also lateral interactions among disturbances. This paper examines a robust case of wave-merger cyclogenesis, with emphasis on diagnosing both lateral and vertical interactions between disturbances.

Corresponding author address: Gregory J. Hakim, Department of Atmospheric Science, ES-221, State University of New York at Albany, Albany, NY 12222.
E-mail: greg@atmos.albany.edu

The case chosen for analysis occurred on 25–26 January 1978 over the Ohio Valley of the United States (aka the "Cleveland superbomb"). Synoptic aspects of this case have been documented by Anthes and Keyser (1979), Burrows et al. (1979), Salmon and Smith (1980), and Hakim et al. (1995) (hereafter HBK). Prominent in this case are two localized, large-amplitude disturbances, which appear as depressions of the tropopause. HBK document and interpret this case within the "potential vorticity thinking" (PVT) framework (HMR) and raise issues requiring further clarification. Specifically, they indicate the need to quantify the effects that the upper-level disturbances exert on each other (lateral interactions), the individual contributions of the upper-level disturbances to surface cyclogenesis (vertical interactions), and the effect of the background flow upon the upper-level disturbances, along with its contribution to surface cyclogenesis.

Diagnosis of observed data is crucial in verifying extant theories and in exposing new avenues of research. Advances may occur more rapidly in a framework where observations and theory have a common ground for communication. The common ground in recent years has been the PVT paradigm of HMR, which requires only the potential vorticity (PV) to describe development. Central to this description are the conservation and invertibility properties of PV for flows that are balanced, adiabatic, and frictionless. The invertibility principle is an especially powerful diagnostic tool, since it provides a means of attributing causative effects to limited portions of the atmosphere. This method of diagnosis is chosen in the present paper to isolate the lateral and vertical interactions that contribute to the evolution of the Cleveland superbomb.

The power of the invertibility principle for diagnosing observed cyclogenesis is demonstrated convincingly by Davis and Emanuel (1991). Using the nonlinear balance system, they perform static inversions of an approximate form of the Ertel PV (EPV) in a piecewise manner. Davis and Emanuel infer interactions between upper- and lower-level disturbances through diagnosis of the induced flows attributable to these respective features. In addition, they quantify the contribution of latent heat release to the surface circulation. A similar approach is taken here using the quasigeostrophic (QG) system. Both static and prognostic inversions are performed to elicit the fundamental dynamics of this case of trough merger. Here, the prognostic inversion consists of an application of the well-known height tendency equation from QG theory.

Another issue that must be confronted in the diagnosis and interpretation of observations is the separation of disturbances ("anomalies") from the flow that contains them. For localized disturbances in a background flow, such as the ones studied here, a wave formalism is cumbersome, given the large number of harmonics necessary to describe the structure of such disturbances and the inherent problem of distinguishing

between disturbances and the background flow in the wavenumber domain. A subjective approach for isolating disturbances in the quasigeostrophic potential vorticity (QGPV) field is adopted here. Results shown in section 4 indicate that these disturbances can be viewed as baroclinic vortices. The highly localized structure of these disturbances and the apparent lack of substantial dispersion for 10 days prior to cyclogenesis support a vortex interpretation for these disturbances (Figs. 2 and 3 in HBK).

A description of the data sources for this study follows in section 2. The methodology for both the static and prognostic inversions is described in section 3; the results of the static (prognostic) inversions are presented in section 4 (5). The sensitivity of the solutions to boundary conditions is also explored in section 4, where it is shown that a partition involving interior QGPV and surface potential temperature is problematic and ill-posed in certain situations. The fundamental signatures found in the QGPV inversions are used to motivate a very simple barotropic model of vortex-patch behavior in section 6. For realistic parameters, observed behavior is replicated, but this behavior is found to depend very sensitively on the initial conditions. This sensitivity, along with its implications for operational forecasting of the vortex-merger phenomenon, are discussed. Conclusions are drawn in section 7.

2. Data source

Data for the period between 0000 UTC 23 January and 1200 UTC 27 January 1978 are available at 6-h intervals from a special run of the four-dimensional data assimilation system operational during 1987 at the European Centre for Medium-Range Weather Forecasts (ECMWF) (Hollingsworth et al. 1986), provided courtesy of Dr. Adrian Simmons. These data are stored in spherical harmonic form with T106 resolution in the horizontal and 20 hybrid σ-coordinate levels in the vertical; they are transformed to a 1° × 1° latitude–longitude grid, extending between 11°–89°N and 160°–20°W, and interpolated to 20 equally spaced pressure levels between 1000 and 50 hPa. Minor corrections are introduced to the interpolated temperature field to ensure hydrostatic consistency with the geopotential height field.

3. Methodology

To assess quantitatively the individual roles of the precursor disturbances constituting this case, the total flow field needs to be partitioned in a dynamically meaningful way. Although there are a number of approaches that accomplish this task, one encapsulating the full hydrodynamics and thermodynamics in a single scalar quantity is PV inversion. The goal of this approach is to separate a PV field into pieces, and to associate with each piece a wind and a mass field. We
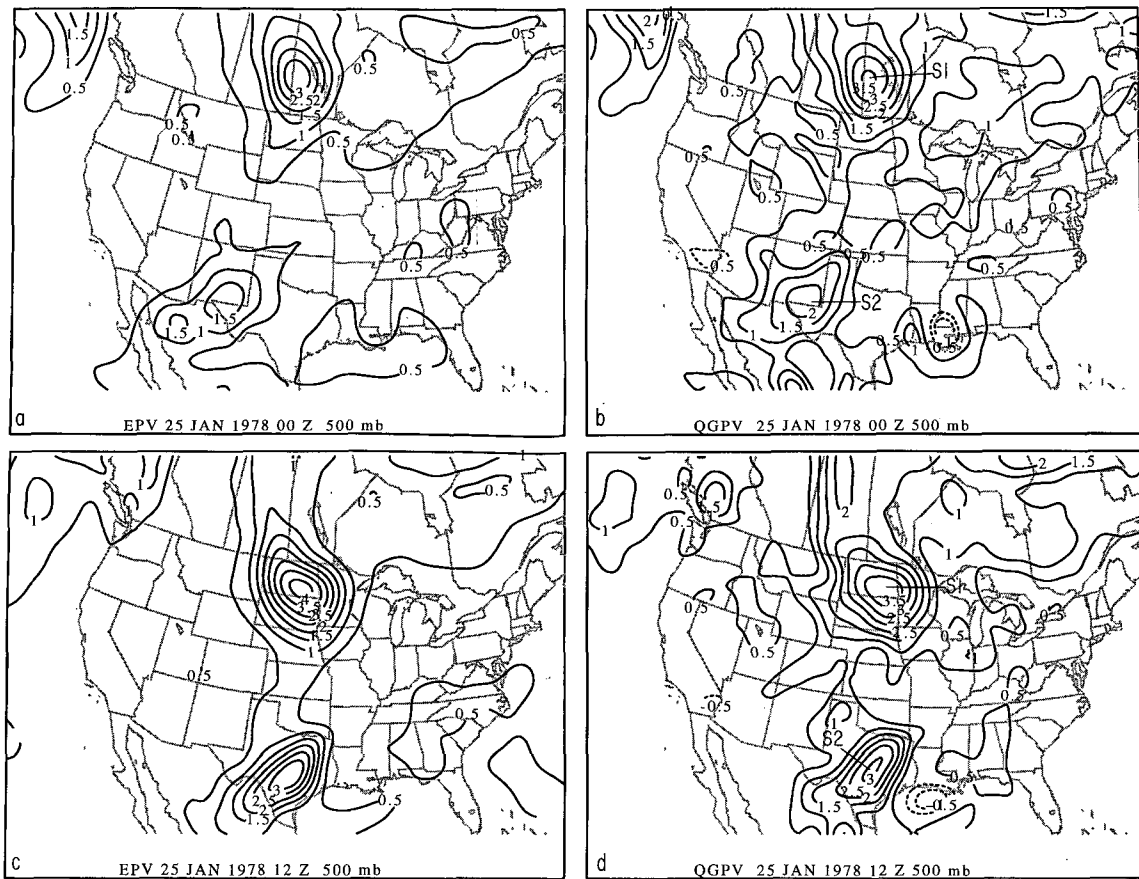
FIG. 1. Comparison of EPV (panels a, c, e, g, and i) and QGPV (panels b, d, f, h, and j) at 500 hPa: 25/00 (a, b), 25/12 (c, d), 26/00 (e, f), 26/12 (g, h), and 27/00 (i, j). Both PV fields are contoured in conventional PV units (1 PVU $= 10^{-6}$ m^2 K kg^{-1} s^{-1}).

refer to this separation procedure, which will be for-
mulated in terms of the QGPV, as piecewise static PV
inversion. In theory, such a separation provides a
framework to quantify interactions between discrete
portions of a fluid and, hence, cause and effect through
near- and far-field interactions. We quantify these in-
teractions in terms of partitioned geopotential height
tendencies using the results of the piecewise static PV
inversions, and refer to this latter procedure as piece-
wise prognostic PV inversion. Piecewise prognostic PV
inversion goes a step beyond performing conventional
diagnostic calculations of QG height tendencies using
total (unpartitioned) fields and then qualitatively at-
tributing the results to particular features within the
flow. We now discuss some general properties of PV
inversion systems and then proceed to outline the
piecewise static and prognostic PV inversions used to
diagnose the present case.

a. PV inversion systems

Since any EPV distribution can be associated with
an arbitrary number of wind and mass fields, it is nec-

essary to specify a balance condition that relates these
fields. In general, the streamfunction for some balanced
system of equations is obtained by inverting the PV
consistent with that system, which will be only an ap-
proximation to the true EPV. For balance conditions in
which the relationship between the PV and stream-
function is linear, the individual contributions to the
streamfunction associated with respective pieces of the
PV field can be superposed to obtain the full stream-
function. Here, the inversion relation provides a one-
to-one mapping of discrete portions of the PV onto a
streamfunction for a given specification of boundary
conditions. Balanced systems that involve a nonlinear
relationship between the PV and the streamfunction
must be linearized to enable superposition of solutions.
In the case of a nonlinear balance condition, the map-
ping onto the streamfunction is not unique for a discrete
portion of PV owing to the arbitrariness involved in the
linearization.

As a practical matter, it would seem that for cases
involving nonnegligible Rossby number there is an in-
herent uncertainty in the exact details of the actual wind
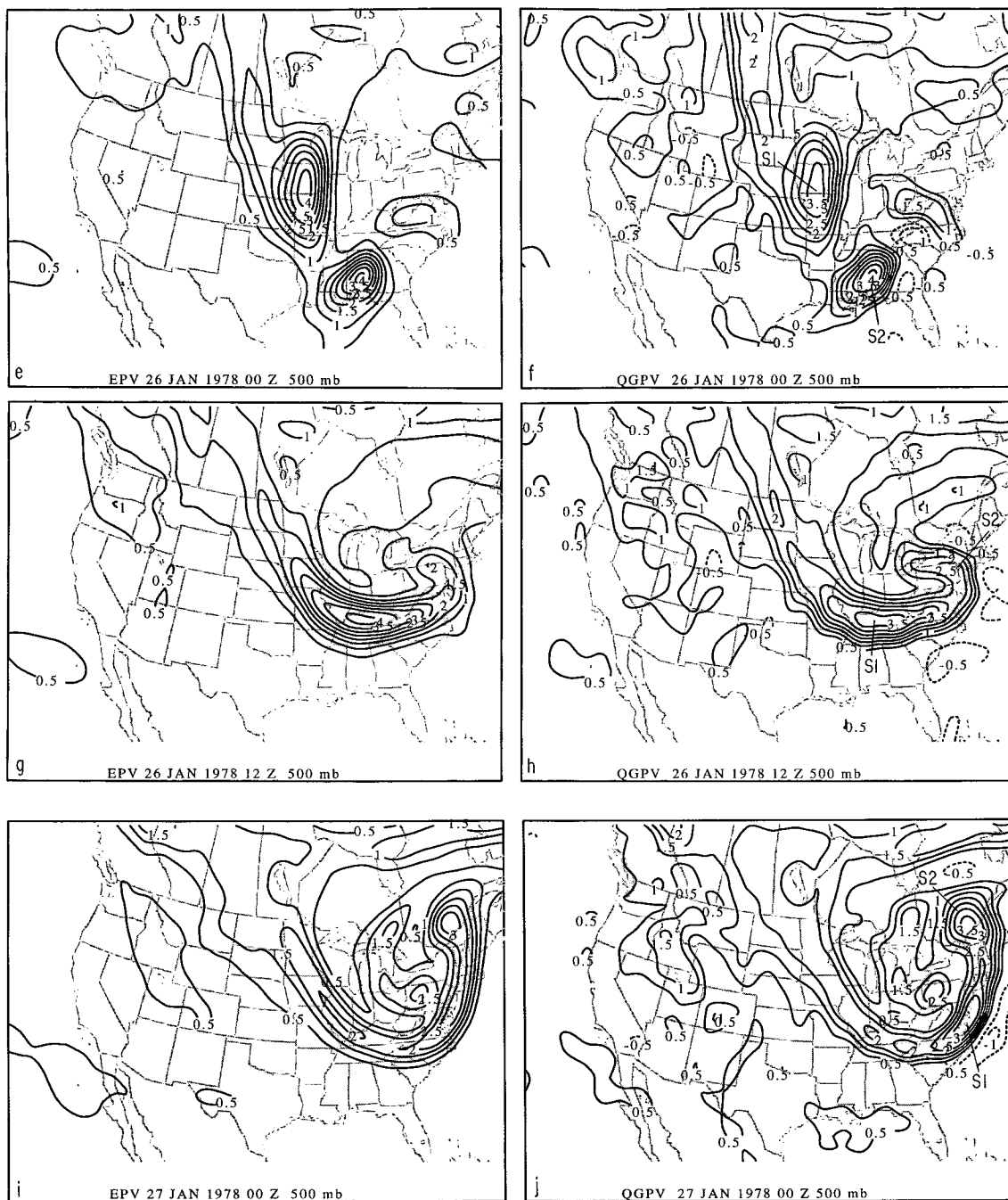and mass fields associated with any discrete subset of

FIG. 1. (Continued)

the total EPV field resulting from two approximations. The first approximation is that of balanced flow, for which the QG system typically will suffer greater error than intermediate models (e.g., McWilliams and Gent 1980). The second approximation involves linearizing a nonlinear operator, which is necessary to permit superposition in most intermediate models. This approx-

imation is not necessary in the QG system, since the QG operator is linear.

Static PV inversion with observed data using an intermediate model has been performed by Davis and Emanuel (1991). Using the nonlinear balance (NB) system, Davis and Emanuel (1991) examine several cases of cyclogenesis and illustrate an interpretation

due to Bretherton (1966) involving interactions between surface- and tropopause-based Rossby waves that result in mutual amplification similar to that in the Eady (1949) model of baroclinic development. Davis (1992a) uses the NB system to diagnose and compare two cases of observed cyclogenesis. Regarding the linearization issue, Davis (1992b, p. 1398) finds that the solutions for several methods of linearizing the NB system in idealized cases vary by less than about 25%.

In pressure coordinates, the QGPV, denoted by q, is given by

$$q = \frac{1}{f_0} \nabla^2 \phi' + f + f_0 \frac{\partial}{\partial p} \left(\frac{1}{\sigma_r} \frac{\partial \phi'}{\partial p} \right). \qquad (1)$$

Here, $\nabla = (\partial/\partial x, \partial/\partial y)$ is the two-dimensional gradient operator in pressure coordinates, ϕ is the geopotential, and f is the Coriolis parameter ($f_0 = 10^{-4} \text{ s}^{-1}$). The static stability coefficient, $\sigma_r = -h(d\theta_r/dp)$, pertains to a reference atmosphere, taken to be the U.S. standard atmosphere, and $h = \alpha/\theta$ is a function of pressure only. The prime symbol in (1) denotes deviations from this reference atmosphere. QGPV inversion has been performed on observed data by Robinson (1988) for flow in the stratosphere and mesosphere, by Holopainen and Kaurola (1991) for planetary-scale flow over the Northern Hemisphere extratropical troposphere, and by Black and Dole (1993) for large-scale tropospheric cyclogenesis over the North Pacific Ocean.

For situations with nonnegligible ageostrophic winds, such as the case to be considered here, application of the QG system may seem questionable. Formally, the QG system is valid only for small–Rossby number flows. Thus, errors will occur in attributing wind and mass fields to discrete regions of PV for situations deviating from small Rossby number. Nevertheless, useful information still may be obtained from QGPV inversion for cases with large Rossby number, provided that the relevant structure in the QGPV field correlates well with the EPV field (Davis 1992b). Indeed, it is conceivable that even for Rossby numbers locally greater than unity the QGPV field still could be highly correlated with the EPV field. In view of this consideration, we prefer to use the QG system in an attempt to elicit the essence of the dynamics for this case of trough merger, because it facilitates direct comparison with theory and its operator is linear.

A comparison of EPV and QGPV [scaled by $-g(d\theta_r/dp)$] at 500 hPa for the ECMWF dataset in this case is given in Fig. 1. At 0000 UTC 25 January 1978 (25/00), the two precursor disturbances, referred to as S1 and S2, are located over south-central Canada and extreme western Texas, respectively, in both the EPV and QGPV fields (Figs. 1a,b). By 25/12, both the EPV and QGPV show an increase of the PV values in S2 to 3 PVU (Figs. 1c,d). Note the encouraging similarity between the EPV and QGPV in terms of the

scale and orientation of S1 and S2, as well as the gradients near the edges of these features. The subsequent evolution continues to show a remarkable similarity between the EPV and QGPV. As the two prominent precursors of large EPV and QGPV come together over the Ohio Valley (Figs. 1e–h), an intense surface-based cyclone develops. This cyclone deepens from 998 to 955 hPa between 25/12 and 26/12, as it tracks from the Gulf of Mexico coast to southern Ontario during this period (HBK, section 5). At 27/00, the PV fields exhibit the signature of a "breaking wave" surrounding the location of the surface cyclone (Figs. 1i,j); the two precursor disturbances are evident within this wave signature.

Overall, the QGPV field clearly mimics the position, alignment, and gradients in the EPV field associated with the two systems of interest in this case. Even mesoscale features, such as the small blobs in the EPV field north of Lake Huron and over western Pennsylvania at 27/00, are represented in the QGPV field (Figs. 1i,j). Table 1 lists the correlation coefficients between EPV and QGPV at 500 hPa, as well as for all pressure levels within the data volume defined in section 2. Correlations between 0.8 and 0.9 quantitatively confirm the visual correspondence between these fields.

Although both the EPV and QGPV fields in Fig. 1 imply that the upper precursors S1 and S2 are localized, large-amplitude disturbances at 500 hPa, this pressure level is not a material surface for flows described by the adiabatic, frictionless primitive equations. However, analyses of the dynamic tropopause, a genuine material surface, show that these disturbances comprise regions of closed potential temperature contours and that they translate conservatively (HBK, section 4); that is, they exhibit the properties of material eddies rather than of finite-amplitude waves on a background PV gradient. This distinction suggests that the upper precursors may be interpreted as baroclinic vortices with maximum amplitude near the tropopause. This interpretation of disturbance structure will be addressed

TABLE 1. Correlation coefficients between distributions of EPV and QGPV. The left column gives the date/time, the middle column the correlation coefficient at 500 hPa, and the right column the correlation coefficient for all pressure levels within the data volume defined in section 2.

Date/time	500 hPa	All levels
25/00	0.81	0.87
25/06	0.80	0.88
25/12	0.81	0.87
25/18	0.81	0.86
26/00	0.82	0.86
26/06	0.82	0.85
26/12	0.84	0.84
26/18	0.85	0.83
27/00	0.86	0.82

subsequently through piecewise static inversion of QGPV.

b. Piecewise static QGPV inversion

Given the QGPV field as defined in (1), piecewise static inversion is performed by inverting discrete portions of this field subject to appropriate boundary conditions. The partial differential equation (1) can be expressed as an operator and source function (HMR):

$$\mathcal{L}(\phi') = q_*, \tag{2}$$

where the operator is defined as

$$\mathcal{L} \equiv \frac{1}{f_0} \nabla^2 + f_0 \frac{\partial}{\partial p} \left(\frac{1}{\sigma_r} \frac{\partial}{\partial p} \right) \tag{3}$$

and $q_* \equiv q - f$. For a q_* field partitioned into n pieces, such that $q_* = \Sigma_{i=1}^n q_{*i}$, the perturbation geopotential associated with the ith piece is obtained by the inverse mapping,

$$\phi_i' = \mathcal{L}^{-1}(q_{*i}), \tag{4}$$

such that $\phi' = \Sigma_{i=1}^n \phi_i'$. A limited-area domain consisting of a subset of the $1° \times 1°$ latitude–longitude grid described in section 2, extending between $11°–75°N$ and $151°–31°W$, is used for all static as well as prognostic inversion calculations. Because a number of issues arise in the selection of boundary conditions for the static inversions, discussion of these conditions is deferred to section 4a.

c. Piecewise prognostic QGPV inversion

Prognostic inversion is achieved using the partitioned geostrophic winds obtained from the static inversion to advect the full QGPV field:

$$\left(\frac{\partial \phi'}{\partial t} \right)_i = \mathcal{L}^{-1}(-\mathbf{V}_{gi} \cdot \nabla q), \tag{5}$$

where

$$\mathbf{V}_{gi} = \frac{1}{f_0} \mathbf{k} \times \nabla \phi_i' \tag{6}$$

is the geostrophic wind associated with the ith piece of the perturbation geopotential field obtained from the static inversion. For the present inversions, the full QG perturbation geopotential tendency is given by $\Sigma_{i=1}^n (\partial \phi'/\partial t)_i$. The horizontal boundary conditions for the prognostic inversions are obtained through the QG thermodynamic equation for each element ϕ_i', assuming zero vertical velocity at the lower and upper boundaries:

$$\frac{\partial}{\partial p} \left(\frac{\partial \phi'}{\partial t} \right)_i = -h(-\mathbf{V}_{gi} \cdot \nabla \theta'), \tag{7}$$

where θ' is the perturbation potential temperature, obtained from the perturbation thickness of the 50-hPa-

deep layers adjacent to the horizontal boundaries. Further discussion of the specification of boundary conditions for the prognostic inversions is deferred to section 5.

There are many limitations to the static and prognostic approaches outlined above. Among them are the QG approximation for a situation with nonnegligible Rossby number (distributions not shown). The contributions of topographic, frictional, and diabatic forcings to the prognostic inversions are neglected. Using a limited-area domain reduces computational demand; however, this approach introduces lateral boundary conditions and, thus, an inherent arbitrariness to the partitioned solutions. With the aforementioned caveats, it is emphasized that we are attempting to obtain the "essence" of the dynamical influence of, and interactions between, the individual systems in this case within a consistent framework, rather than achieve a higher degree of accuracy at the cost of increased conceptual and numerical complexity. A discussion of boundary conditions for and results from the static inversions follows.

4. Piecewise static QGPV inversions

A significant issue related to the mechanics of PV inversion is partitioning the PV field. One method involves temporal filtering of data, typically into a time-mean or a slowly varying background field and a perturbation field. The evolution of disturbances obtained by this method can be compared directly with theory. However, unlike modes in linear theory, which are formally separable from the basic state, real disturbances evolve and interact nonlinearly with the basic state. As described by HBK (section 4), the present case involves localized, large-amplitude disturbances S1 and S2, which are based at the tropopause and extend downward to nearly 800 hPa prior to the development of the surface cyclone. In view of the complications arising in the application of conventional (i.e., Fourier) spatial filtering techniques to such disturbances, we adopt the pragmatic approach of extracting these disturbances by inverting the full q_* fields identified with the localized features S1 and S2. Limited volumes are chosen for inversion by selecting the last closed contours of 500 hPa QGPV (using a 0.5-PVU contour interval) encompassing S1 and S2, respectively. The areas enclosed by these contours are extended vertically to the top and bottom of the domain. Although this method of isolating the QGPV distributions associated with S1 and S2 is subjective and arbitrary, preliminary tests with limited volumes encompassing larger geographical regions yield results similar to those to be presented subsequently. The q_* field exterior to S1 and S2 is associated with the background flow.

The situation posed by the present case requires inversion of the respective distributions of q_* associated

with S1 and S2, the domain average of which is non-zero for each distribution. The traditional boundary condition for piecewise inversion of the q_* field consists of zero perturbation potential temperature on the horizontal boundaries (e.g., HMR, pp. 903–905, their Fig. 15). This boundary condition derives from the classic Eady problem of baroclinic development, where wavelike disturbances on horizontal boundaries representing the tropopause and ground mutually amplify while propagating on opposing PV (i.e., boundary potential temperature) gradients. When interior PV anomalies are considered in the Eady framework, they are associated with zero (perturbation) potential temperature on the horizontal boundaries. Thus, the traditional boundary condition assumes a separation between interior PV anomalies and boundary potential temperature distributions. As will be demonstrated in the following section, conceptual difficulties arise when considering the traditional boundary condition in the context of the present problem, requiring adoption of an alternative set of boundary conditions. These difficulties motivate a comprehensive examination of admissible sets of boundary conditions for the piecewise static inversion problem and their impact on solutions attributed to localized regions of q_*, such as S1 and S2.

a. Integral constraint and boundary conditions

The goal in solving (4) is to attribute wind and mass fields to a portion of the full q_* field. Unfortunately, the results of this endeavor are sensitive to the boundary conditions that must be imposed to obtain these fields. Since there is no unambiguous method for partitioning the boundary conditions, there exists a range of mathematically consistent possibilities. This is an example of the "attribution problem," as formulated by Bishop and Thorpe (1994). As an illustration of the difficulties involved, consider the integral constraint that arises directly from q_* when it is expressed as the divergence of a vector field (Bishop and Thorpe 1994). In pressure coordinates this expression is given by

$$q_* = \nabla_3 \cdot \mathbf{D}, \qquad (8)$$

where

$$\mathbf{D} = \left(\frac{1}{f_0} \frac{\partial \phi'}{\partial x}, \frac{1}{f_0} \frac{\partial \phi'}{\partial y}, -f_0 \frac{\theta'}{d\theta_r/dp} \right), \qquad (9)$$

and

$$\nabla_3 = \left(\frac{\partial}{\partial x}, \frac{\partial}{\partial y}, -\frac{\partial}{\partial p} \right). \qquad (10)$$

Applying the divergence theorem to a volume integral of q_* yields

$$\int_V q_* dV = \int_S \mathbf{D} \cdot \mathbf{n} dA, \qquad (11)$$

where $\mathbf{n}$ is a unit vector oriented outward from the surface S that bounds volume V. Expanding (11) yields

$$\int_V q_* dV = \int_{A_1} \frac{f_0 \theta'_1}{(d\theta_r/dp)_1} dA_1$$

$$- \int_{A_2} \frac{f_0 \theta'_2}{(d\theta_r/dp)_2} dA_2 + \int_{A_3} \mathbf{D} \cdot \mathbf{n} dA_3. \qquad (12)$$

Here, subscripts 1 and 2 denote the lower and upper horizontal boundaries, respectively, and 3 denotes the vertical boundaries. Figure 2 shows a schematic of the geometry of the domain under consideration and boundary definitions. In the absence of vertical boundaries, the third term on the right-hand side of (12) disappears; if the volume integral of q_* is positive, the following inequality must be satisfied:

$$\overline{\theta'_1} < \overline{\theta'_2} \left(\frac{A_2}{A_1} \right) \frac{(d\theta_r/dp)_1}{(d\theta_r/dp)_2}. \qquad (13)$$

Overbars in (13) denote area averages of θ' over A_1 and A_2. Consider the special case of Cartesian geometry and assume a uniform reference state, so that A_2/A_1 and $(d\theta_r/dp)_1(d\theta_r/dp)_2^{-1}$ reduce to unity. Under these circumstances, the lower surface must on average be "colder" than the upper surface. Clearly, the distributions of perturbation potential temperature on the upper and lower horizontal boundaries cannot be interpreted as being dynamically distinct from the volume integral of q_*. This suggests that the traditional boundary condition in PVT as proposed by HMR, involving a partition between interior PV and surface potential temperature, is questionable in general; related concerns also have been raised by Green (1987), Holopainen and Kaurola (1991), and Bishop and Thorpe (1994).
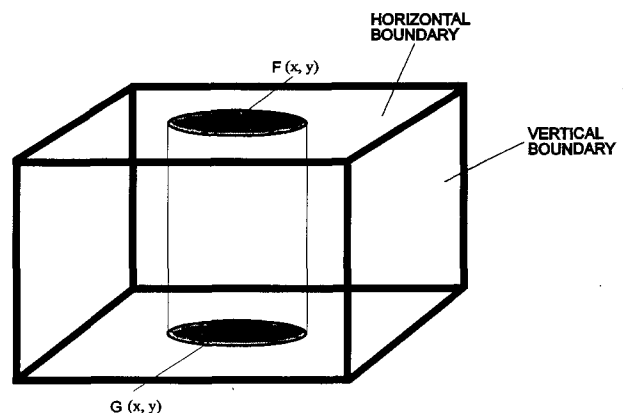

FIG. 2. Schematic illustration of the computational domain. Vertical and horizontal boundaries are shown, as well as one of the volumes over which q_* is inverted (i.e., S1 and S2). Functions $F(x, y)$ and $G(x, y)$ represent boundary conditions on the shaded regions; these are defined for the various inversions in Table 2.

Equation (12) also imposes a constraint on the area-integrated geostrophic winds tangential to the vertical boundaries of an arbitrary volume. For example, consider such a volume containing positive q_* and insist that the associated perturbation potential temperature vanishes on the horizontal boundaries (as in PVT). In this situation, the first and second terms on the right-hand side of (12) are zero and the third term must satisfy the volume integral. Here, the integrated effect of the horizontal winds tangential to the vertical boundaries must be a cyclonic circulation consistent with the positive volume integral of q_*. When all three terms on the right-hand side of (12) contribute to the integral over an arbitrary volume containing positive q_*, the bounding surfaces of that volume exhibit the same characteristics anticipated by PVT in the vicinity of a cyclonic QGPV anomaly: a cold anomaly below, a warm anomaly above, and cyclonic circulation (HMR, 903–905). Similarly, volume integrals of negative q_* are associated with a warm anomaly below, a cold anomaly above, and anticyclonic circulation.

This brings us to the crux of the problem for piecewise static inversion: How are the boundary conditions to be formulated a priori? The traditional approach in PVT assumes homogeneous Neumann horizontal boundary conditions (specification of perturbation potential temperature) when inverting the interior q_*, and inhomogeneous Neumann horizontal boundary conditions, along with zero interior q_*, when inverting the perturbation potential temperature on the lower and upper boundaries (Bretherton 1966; HMR; Thorpe 1986; Davis and Emanuel 1991). Given the constraint (12), the traditional approach clearly is ill posed when applied to global or periodic domains under the following circumstances: 1) nonzero volume-integrated q_* in the domain interior, along with homogeneous Neumann horizontal boundary conditions; 2) nonzero area-integrated perturbation potential temperature on the horizontal boundaries, along with zero interior q_*. For limited-area domains (e.g., Fig. 2), however, use of homogeneous Dirichlet conditions on the vertical boundaries in these two inversions ensures that (12) is satisfied automatically (through the third term on the right-hand side) by allowing sufficient horizontal circulation along the vertical boundaries.

Alternatively, use of homogeneous Dirichlet conditions (specification of perturbation geopotential) on all boundaries of limited-area domains permits a solution for perturbation potential temperature on the lower and upper boundaries and horizontal winds tangential to the vertical boundaries for a given distribution of interior q_*. This approach does not associate any flow on the horizontal boundaries, nor any perturbation potential temperature on the vertical boundaries, with the interior q_*. This choice of boundary conditions attributes the upper- and lower-boundary flow and the vertical-boundary perturbation potential temperature to q_* exterior to the domain or on the domain boundaries. An

important property of this approach that distinguishes it from its traditional counterpart is that it does not place restrictions on any of the terms contributing to (12).

For a given nonzero volume integral of q_*, the aforementioned alternatives of homogeneous Neumann and Dirichlet conditions on the horizontal boundaries in conjunction with homogeneous Dirichlet conditions on the vertical boundaries shift emphasis from horizontal winds tangential to the vertical boundaries to perturbation potential temperature on the horizontal boundaries. Consideration of (12) indicates that this shift in emphasis is in fact optimized for the following combinations of boundary conditions: 1) homogeneous Neumann conditions on the horizontal boundaries and homogeneous Dirichlet conditions on the vertical boundaries; 2) homogeneous Dirichlet conditions on the horizontal boundaries and homogeneous Neumann conditions on the vertical boundaries. In other words, these respective combinations of boundary conditions exchange vorticity and perturbation static stability in a domain-integrated sense as required by (12). The choice of boundary conditions therefore biases dynamical interpretations that depend on the relative contributions of the horizontal wind and perturbation potential temperature fields attributed to a discrete region of q_*.

Bishop and Thorpe (1994) propose a domain-independent form of PVT through the use of the free-space Green's function for the QG operator with constant coefficients. Since the streamfunction and its gradient for the free-space Green's function decay with distance to zero at infinity, both the streamfunction and its normal gradient are nonzero on all boundaries of limited-area domains. However, complications arise when the reference state is not uniform. The variable coefficient in the static stability portion of the QG operator (3) then acts to distort the classic Green's function solution, which Bishop and Thorpe equate with the bound charge that appears when electric charges are situated within dielectric media. In addition, to solve a problem completely with this approach, arbitrary assumptions about the reference state beyond the boundaries of the domain are required. Consequently, the uncertainties arising from these assumptions and their impact on the solution may be as large as those in bounded-domain solutions. Despite these uncertainties, we include the free-space Green's function solutions in the upcoming comparison of alternative boundary condition formulations, since, by virtue of yielding both perturbation potential temperature and geostrophic wind on the horizontal boundaries, these solutions provide an objective basis for assessing the influence of the various boundary condition formulations on the piecewise static inversions of S1 and S2.

In the static inversions performed here that require boundary conditions, homogeneous Dirichlet conditions are specified on the vertical boundaries when inverting q_* associated with S1 and S2. The q_* distri-

butions associated with S1 and S2 are inverted individually, with $q_* = 0$ outside these respective regions. Three options for the horizontal boundary conditions are adopted; these are detailed in Table 2. The homogeneous Dirichlet (DH) option yields a perturbation potential temperature signature on the upper and lower boundaries of S1 and S2, but no geostrophic wind signature on these boundaries. Conversely, the homogeneous Neumann (NH) option yields a geostrophic wind signature on the upper and lower boundaries of S1 and S2, but no perturbation potential temperature signature on these boundaries. Hybrid conditions, referred to as inhomogeneous Neumann (NI), provide an option that allows both geostrophic wind and perturbation potential temperature signatures on the horizontal boundaries of S1 and S2. For the NI inversions, homogeneous Neumann conditions are imposed on the horizontal boundaries everywhere except in the regions enclosed by the prescribed boundaries of S1 and S2 for the respective inversions. The NI option effectively associates all (none) of the horizontal boundary perturbation potential temperature inside (outside) the S1 and S2 boundaries to q_* within these volumes. Free-space Green's function (GF) solutions are obtained for a reference state with a constant value of the static stability parameter, $\sigma_r = 4.84 \times 10^{-6}\ \text{m}^4\ \text{s}^2\ \text{kg}^{-2}$, characteristic of the troposphere of the reference-state atmosphere adopted in section 3a. The specific form of the solution is given by Eq. (6) in Bishop and Thorpe (1994). Finally, the background flow for all of the static inversions is obtained by subtracting the sum of the perturbation geopotential height fields associated with S1 and S2 from the analyzed geopotential height field.

Examples of the static inversions are shown for S1 at 25/12 in Fig. 3 for 500 hPa and in Fig. 4 for 1000 hPa. At 500 hPa, all solutions yield a perturbation geopotential monopole centered over North Dakota, with winds decreasing with increasing distance away from S1. However, there are substantial differences in the amplitude and in the wind fields for the different boundary conditions. For any given distance from the center of S1, the NH inversion yields the strongest winds (Fig. 3b). This result illustrates the compensation in vertical-boundary tangential winds in the absence of surface perturbation potential temperature, necessary to satisfy (12). Differences between the solutions are even more pronounced at 1000 hPa (Fig. 4). The NH results at 1000 hPa exhibit an intense cyclonic vortex, while the others show much weaker circulations. The zero wind field in the DH results is in closer agreement with the GF results than with the wind field in the NH results, the maximum speed of which exceeds 50 m s^{-1}. The close agreement between the DH and GF results at 1000 hPa suggests that the Dirichlet condition is more "realistic" than NH and less prone to cancellation with the perturbation geopotential height field associated with the background flow that is

TABLE 2. Horizontal boundary conditions for the static QGPV inversions of S1 and S2. The left column gives the boundary condition type, the middle column the bottom boundary condition, and the right column the top boundary condition. Horizontal boundary conditions are homogeneous everywhere outside of S1 and S2. See Fig. 2 for a schematic illustration of the application of these boundary conditions.

Inversion type	Bottom boundary $[G(x, y)]$	Top boundary $[F(x, y)]$
Homogeneous Dirichlet (DH)	$\phi_b' = 0$	$\phi_t' = 0$
Homogeneous Neumann (NH)	$\left(\dfrac{\partial \phi'}{\partial p}\right)_b = 0$	$\left(\dfrac{\partial \phi'}{\partial p}\right)_t = 0$
Inhomogeneous Neumann (NI)	$\left(\dfrac{\partial \phi'}{\partial p}\right)_b = \left(\dfrac{\partial \phi'}{\partial p}\right)_{obs}$	$\left(\dfrac{\partial \phi'}{\partial p}\right)_t = \left(\dfrac{\partial \phi'}{\partial p}\right)_{obs}$

required to yield the analyzed 1000-hPa perturbation geopotential height field (refer ahead to Fig. 11d).

The question arises whether the differences between solutions resulting from the various boundary condition options presented in Table 2 and illustrated in Figs. 3a–c and 4a–c are an artifact of the nonzero domain average of the q_* distribution associated with S1. By virtue of the presence of the third term on the right-hand side of the integral constraint (12), which requires geostrophic flow tangential to the vertical boundaries to contribute to satisfying the nonzero volume integral of q_* associated with S1, the far-field influence of S1 may be amplified, especially in the NH case. An additional concern is that differences between the solutions are being affected by the proximity of the vertical boundaries, and thus are not purely due to differences in the specification of the horizontal boundary conditions. Results (not shown) of inversions performed on a modified distribution of q_* obtained by subtracting the domain average of q_* from the distribution associated with S1 are very similar to those in Figs. 3a–c and 4a–c. Furthermore, solutions for domains larger than the diagnostic domain are close to those in Figs. 3a–c and 4a–c. Thus, we conclude that differences in the solutions for the various boundary condition options presented in Table 2 result primarily from differences in the horizontal boundary conditions.

Cross sections through the respective solutions illustrate the impact of boundary conditions on the vertical structure. For S1, all four solutions exhibit a baroclinic vortex structure possessing peak amplitude near 400–500 hPa, with a warm anomaly above and cold anomaly below (Fig. 5). The core of the vortex in the NH case extends to 1000 hPa, whereas it is "buffered" by cold ground in the NI case (Figs. 5b,c). At all levels, the magnitude of the wind component normal to the cross section in the NH solution exceeds that in the DH solution. The compensation between the horizontal-boundary perturbation potential temperatures and the vertical-boundary tangential winds for the DH and NH
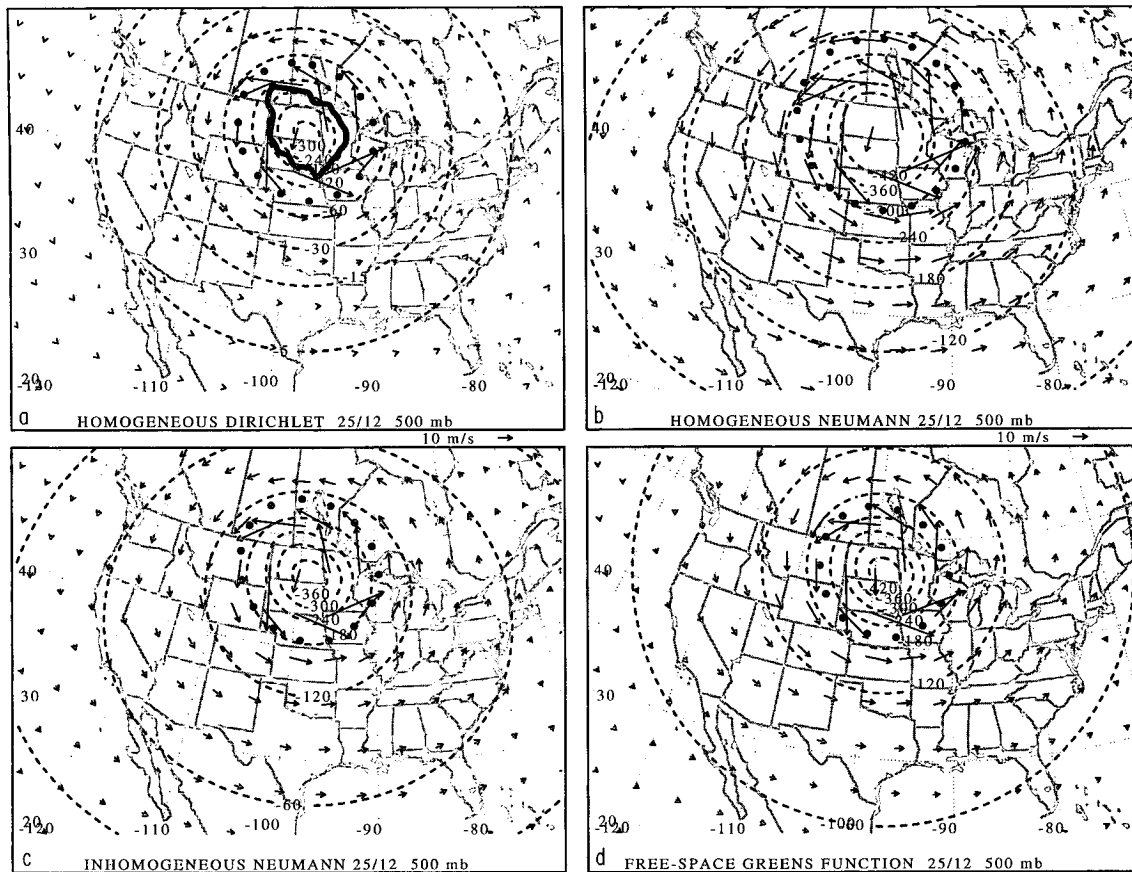
FIG. 3. Static-inversion solutions for S1 at 500 hPa at 25/12. Derived 500-hPa perturbation geopotential height fields (m) and geostrophic winds are shown for the following inversions: (a) homogeneous Dirichlet, (b) homogeneous Neumann, (c) inhomogeneous Neumann, and (d) free-space Green's function. The heavy contour in (a) shows the boundary of the region associated with S1; heavy dots surrounding S1 represent the e-folding distance based on the central value of perturbation geopotential height.

solutions is a striking illustration of the impact of the integral constraint (12) (e.g., cf. the internal structure of the perturbation potential temperature and wind fields within the 1000–500-hPa layer in Figs. 5a,b).

The differences between the DH and NH solutions (Figs. 5a,b) may be understood by recognizing that the constraint (12) applies not only to the solution domain volume, but to all subdomain volumes as well. For example, consider a cylindrical "control volume" centered on S1, extending from the top to the bottom of the domain, with a radius greater than the distance from the center of S1 to the outermost point on its boundary[1] and lesser than the shortest distance to the boundary of the solution domain. The left-hand side of (12) (the volume integral of q_*) is minimized when the vertical boundary of the control volume is at the limits of the

solution domain and increases to a maximum as the vertical boundary of the control volume approaches the edge of S1. For the NH solution, the first two terms on the right-hand side of (12) are everywhere zero [consistent with the specification of zero perturbation potential temperature on the horizontal boundaries (Table 2)], requiring the third term (tangential winds on the vertical boundary of the control volume) to satisfy the volume integral of q_*. Therefore, as the radius of the control volume decreases, the tangential winds on its vertical boundary must increase in a manner consistent with the increase in volume-integrated q_*, reaching a maximum when the vertical boundary approaches the edge of S1. For the DH solution, the first two terms on the right-hand side of (12) are nonzero and thus reduce the burden on the third term, such that weaker tangential winds are required relative to the NH solution on the vertical boundary of the control volume as it approaches the edge of S1.

The GF solution (Fig. 5d) suffers from the lack of a stratosphere, a consequence of the homogeneous ref-

---

[1] Recall from its definition that S1 is not a right circular cylinder. For the present thought experiment, the center of S1 may be defined as the point of maximum 500-hPa QGPV in this feature.
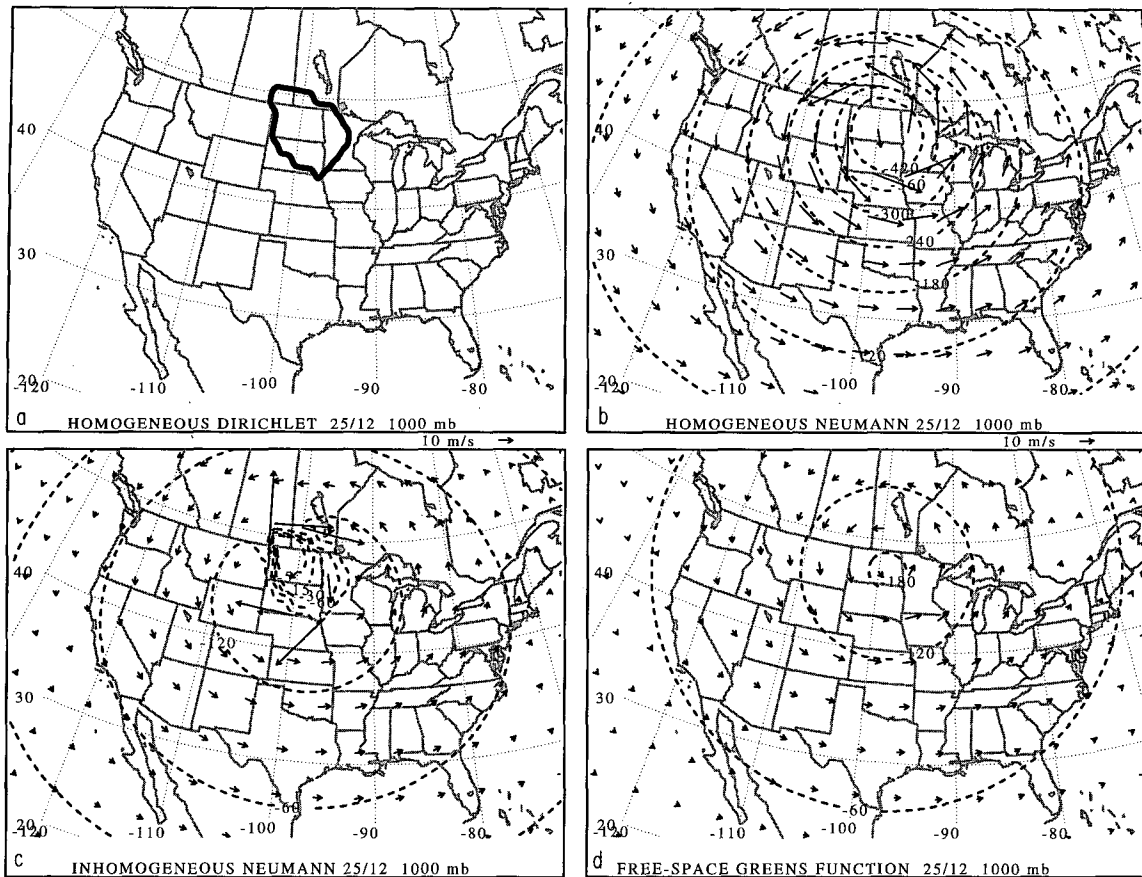
FIG. 4. As in Fig. 3 except for 1000 hPa (e-folding distances not shown).

erence state necessary to obtain the Green's function analytically. However, this solution is the only one that induces *both* wind and perturbation potential temperature fields on all boundaries. The vertical structure of the wind field in the GF solution exhibits a decay from maximum values near 50 m s^{-1} at midlevels to less than 10 m s^{-1} at the lower boundary, and the perturbation potential temperature field shows negative values extending from midlevels to a local minimum near the lower boundary. Although the actual values in the DH solution differ from those in the GF solution, the overall low-level structure is very similar (Figs. 5a,d). Comparing the NI inversion with its GF counterpart indicates that attributing all of the perturbation potential temperature on the lower and upper boundaries of S1 to the distribution of q_* within S1 is unrealistic (Figs. 5c,d). As a consequence of this choice of attribution, the NI solution yields a lower-level (upper-level) perturbation potential temperature field that is too "cold" ("warm") compared with the GF solution for the given distribution of q_* within S1. However, apart from the spurious winds associated with the discontinuities in the lower- and upper-boundary perturbation potential temperatures, the NI results also appear

superior to their NH counterparts. Finally, the NI results reveal the sensitivity of the NH case to changes in the specification of the horizontal boundary conditions for S1. An analogous variation on the DH case (not shown) using analyzed perturbation geopotential values on the upper and lower boundaries of S1 (i.e., inhomogeneous Dirichlet conditions) shows little difference from the DH case. This outcome implies that the DH results are relatively insensitive to changes in the horizontal boundary conditions, suggesting that the Dirichlet option is more robust than the Neumann option. Corresponding inversions for S2 (not shown) also yield a baroclinic vortex structure with peak amplitude near 350–450 hPa and similar differences between the various boundary condition options.

In conclusion, we adopt the DH boundary condition for the static inversions for the remainder of this work for the following reasons:

1) It does not place restrictions on any of the terms contributing to the integral constraint (12).

2) The solutions are less sensitive to changes in the horizontal boundary conditions than in the Neumann alternative.
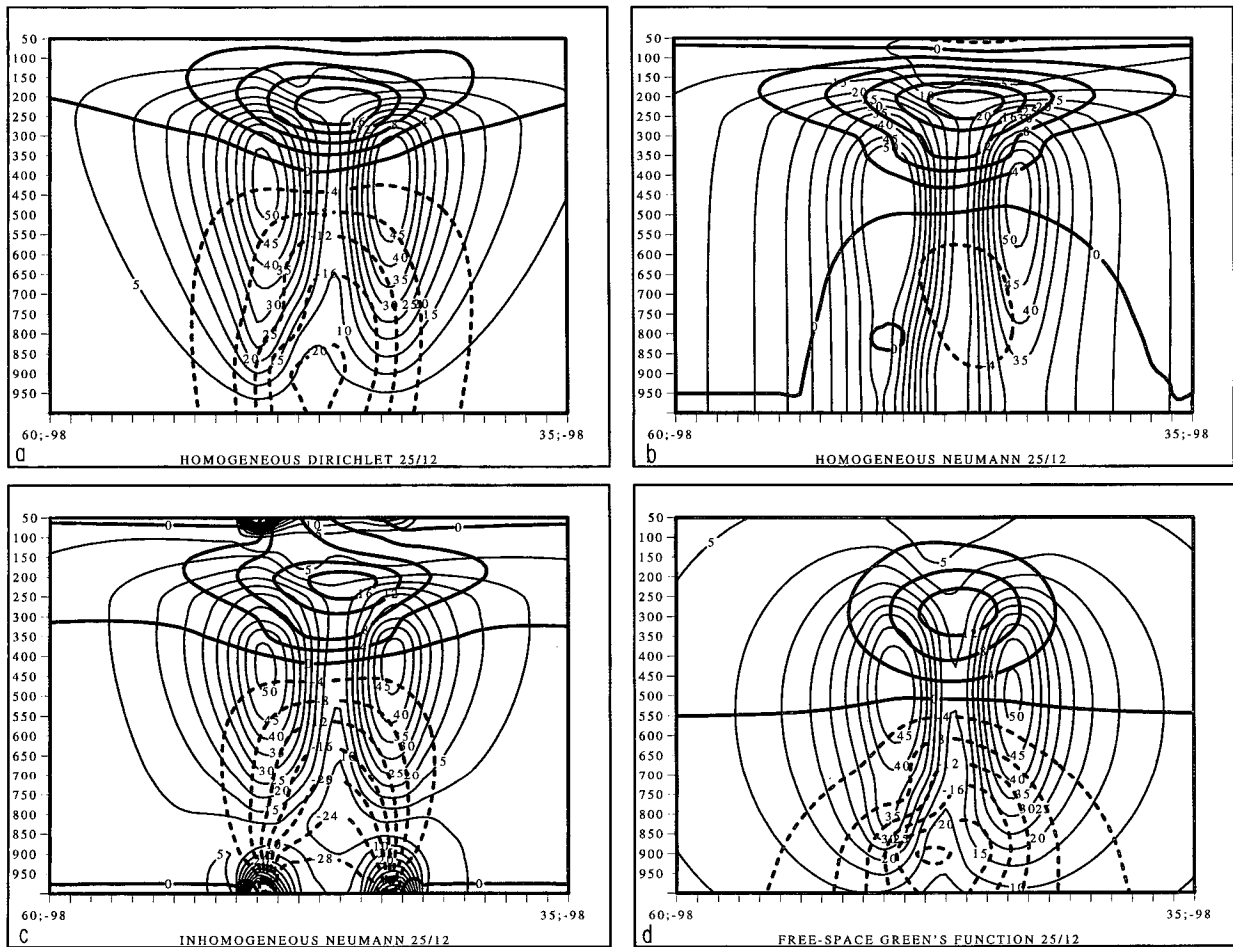
FIG. 5. Cross sections of static-inversion results through S1 at 25/12. Thin solid lines show the magnitude of the geostrophic wind normal to the cross section (m s^{-1}), and thick lines the perturbation potential temperature (K, negative values dashed). The results are shown for the following inversions: (a) homogeneous Dirichlet, (b) homogeneous Neumann, (c) inhomogeneous Neumann, and (d) free-space Green's function. The cross sections are taken along 98°W, with the latitudes and longitudes at the endpoints of the cross sections given on the abscissa.

3) Compared with the Neumann alternative, it is less prone to cancellation required to yield the analyzed perturbation geopotential height fields at the upper and lower boundaries.

4) It yields a three-dimensional structure of wind and perturbation potential temperature consistent with qualitative expectations for a localized upper-level PV anomaly.

5) It compares well with the free-space Green's function alternative.

b. Piecewise PV life cycle

Figures 6 and 7 contain the DH inversion results for S1 and S2, and for the background flow, respectively, at 500 hPa for the period between 25/00 and 27/00. At 25/00, S1 and S2 appear as two distinct vortices (Fig. 6a), with S2 slightly west of S1. A measure of

the "influence" of each of these systems is given by the e-folding distance based on the central value of perturbation geopotential, which is an effective Rossby radius of deformation for these features. In QG theory, the actual Rossby radius is an external parameter that depends only on the reference state:

$$L_R = \frac{NH}{f_0}, \qquad (14)$$

where $N^2 = (g/\theta_0)(d\theta_r/dz)$, and H is a depth scale, typically that of the troposphere. Unlike L_R, the geopotential-based e-folding distance and the strength of the flow at some location away from S1 and S2 depend on the shape and scale of q_* for these features. Thus, for a given amplitude of the q_* field, large-scale features will influence a larger region than will small-scale features: this is a manifestation of the scale effect discussed by HMR (p. 902). Of course, small-scale fea-
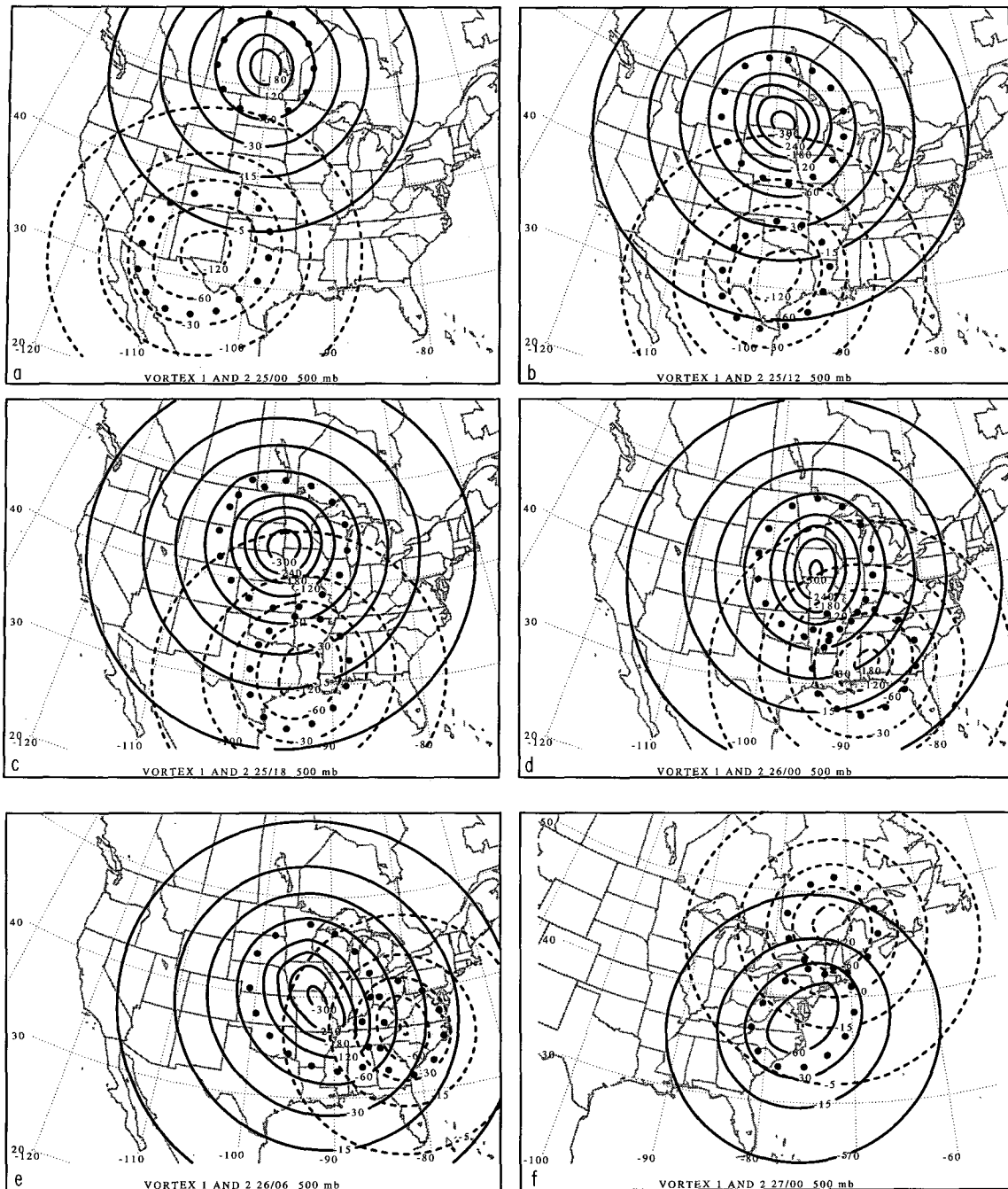
FIG. 6. Plots of perturbation geopotential height (m) at 500 hPa from the inversions of q_* for S1 and S2 at (a) 25/00, (b) 25/12, (c) 25/18, (d) 26/00, (e) 26/06, and (f) 27/00. Solid (dashed) lines are used for S1- (S2-) induced perturbation geopotential height fields. Heavy dots represent the e-folding distance defined as in Fig. 3.

tures having large amplitude may exert much greater influence locally than large-scale features having small amplitude. At 25/00, the lack of appreciable overlap in the e-folding distances indicates that the vortex interactions are weak (Fig. 6a). The background flow appears to dominate the evolution at this time and is act-

ing to advect S1 (S2) southeastward (east-southeastward) (Fig. 7a).

By 25/12, the advections by S1 and the background flow have brought S2 farther east relative to S1 such that S1 and S2 are oriented nearly north–south of each other (Fig. 6b). The amplitude and horizontal scale of
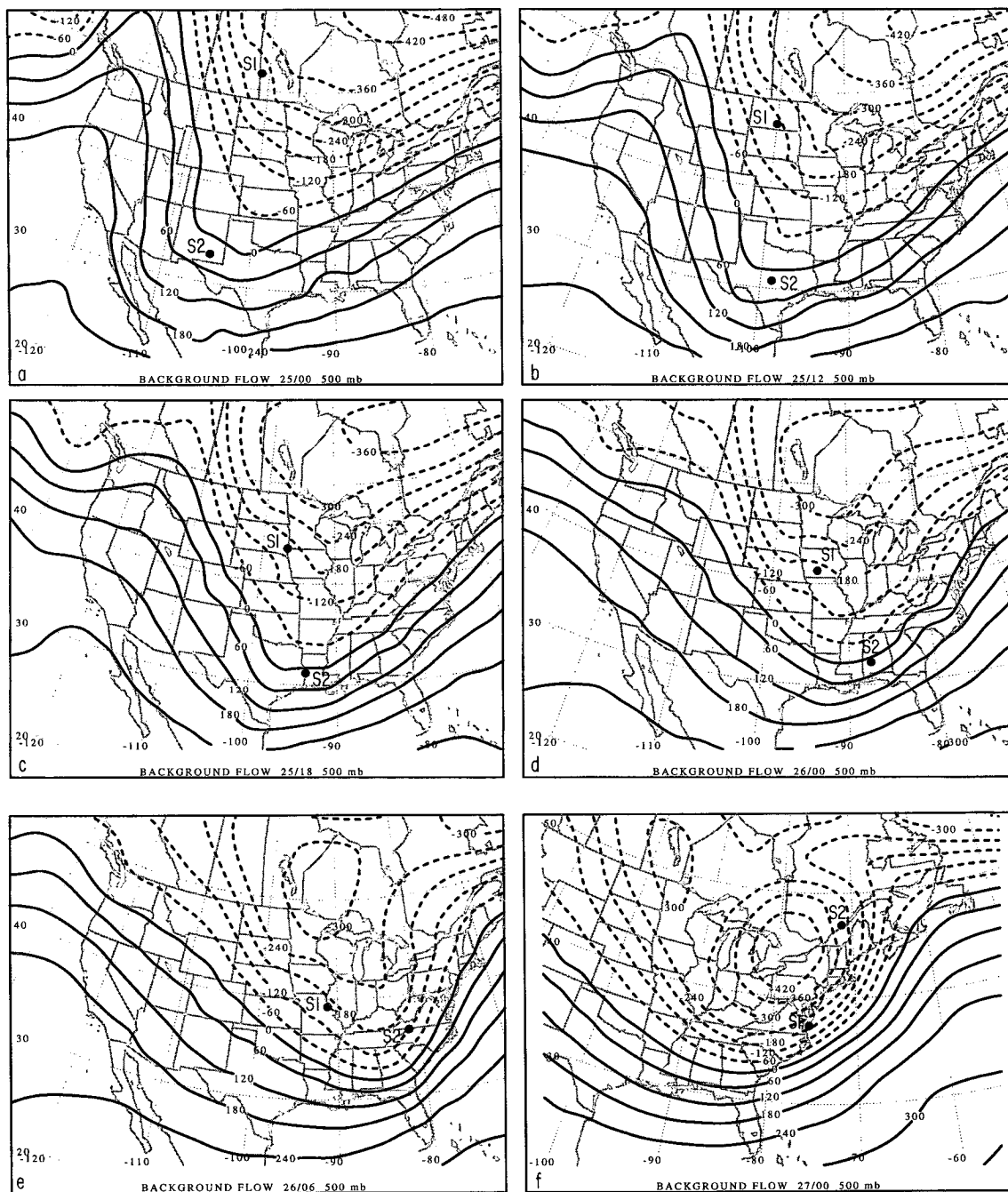
FIG. 7. Plots of perturbation geopotential height (m) at 500 hPa for the background flow at
(a) 25/00, (b) 25/12, (c) 25/18, (d) 26/00, (e) 26/06, and (f) 27/00.

S1 have increased since 25/00 (cf. Figs. 1b and 1d). These changes are reflected in an increase in the central value of the perturbation geopotential and in an enlargement of the area enclosed by the e-folding distance compared to 25/00. The background flow still appears to dominate the motion of each vortex, advecting S1 southeastward and S2 east-northeastward (Fig. 7b).

The background flow continues to bring the vortices closer together at 25/18 (Figs. 6c and 7c). By 26/00, the onset of rapid surface cyclogenesis, overlap of the e-folding distances for S1 and S2 indicates that vortex interactions are quite robust (Fig. 6d), while the background flow continues to bring the two closer together (Fig. 7d). The vortices achieve closest approach at 26/

06 (Fig. 6e), the time of most rapid surface cyclogenesis, and complete a near half-period orbit of each other by 27/00 (Fig. 6f). The background flow exhibits the structure of a synoptic-scale trough with decreasing positive meridional tilt prior to rapid cyclogenesis (Figs. 7a–c) and negative meridional tilt during rapid cyclogenesis (Figs. 7d,e), culminating in a closed circulation center over the occluded surface cyclone by 27/00 (Fig. 7f).

These calculations indicate that this case of trough-merger cyclogenesis may be viewed as a vortex–vortex–background-flow interaction problem. Two cyclonic vortices orbit each other while being brought closer together by a confluent background flow. Although the background flow contains all scales of motion, the dominant signature is that of a synoptic-scale trough evolving from a configuration exhibiting a positive meridional tilt to one that is negative at the onset of rapid surface cyclogenesis. This scale separation is accomplished by the relatively complete extraction of the localized cyclogenesis precursors S1 and S2 by our "ad hoc" spatial filtering technique. The background flow appears to be crucial in this case, since the vortex–vortex interactions are most robust once the vortices have been brought closest together. The time of closest approach, 26/06, coinciding with the time of most rapid cyclogenesis, suggests that the vortex–vortex interactions may be an important contribution to cyclogenesis, as may be the superposition of the vortex flows. In this case, trough merger may be viewed as a close approach of two distinct cyclonic vortices in the QGPV field. The smoothing effect of the QG operator (3) yields a superposition of vortex flows at the time of closest approach that results in a large-amplitude cyclonic circulation and a single trough in the geopotential height field (refer ahead to Fig. 16d).

5. Piecewise prognostic QGPV inversions

The interactions between the vortices and the background flow are now quantified by solving (5) and (7) in a piecewise manner. The wind fields for S1, S2, and the background flow are obtained from the DH static inversions. As a consequence of the DH boundary condition, the wind fields associated with S1 and S2 vanish at the upper and lower boundaries, so that advection of boundary perturbation potential temperature in (7) is due exclusively to the wind field associated with the background flow. The vertical boundary conditions are homogeneous (inhomogeneous) Dirichlet for the prognostic inversions utilizing the wind fields attributed to S1 and S2 (the background flow). The inhomogeneous conditions are obtained by time-centered differencing of the analyzed perturbation geopotential field. It is emphasized that the subscript i on the left-hand sides of (5) and (7) refers to the contributions of the respective flow components associated with S1, S2, and the background flow to the perturbation geopotential tendency.

In other words, the subscript i refers to the perturbation geopotential tendencies induced by S1, S2, and the background flow. These induced tendencies should be distinguished from the tendencies of the respective perturbation geopotential fields associated with S1, S2, and the background flow. For example, although the perturbation geopotential fields associated with S1 and S2 are identically zero for all times at the upper and lower boundaries as a consequence of the DH boundary condition in the static inversions, the perturbation geopotential tendencies induced by S1 and S2 at these boundaries are not necessarily zero by virtue of the form of (7). Although of conceptual interest, the latter alternative, consisting of a prognostic inversion scheme yielding tendencies of the respective perturbation geopotential fields determined from piecewise static PV inversion, is not considered further in the present study.

Before diagnosing the observed case, it is worthwhile to consider qualitatively the dynamics for the simple situation of two cyclonic vortices embedded in an environmental QGPV gradient directed northward and characterized by uniform zonal background flow. Looking first at the vortex–vortex interaction (Fig. 8a), the main contribution of the instantaneous tendencies is cyclonic relative motion of the vortices, such that the southern system moves eastward with the background flow, while the northern system moves westward against the background flow. In addition to the vortex–vortex interaction, there are interactions of the individual vortices with the QGPV associated with the background flow (Fig. 8b). The advection of background QGPV by each vortex will force instantaneous geopotential height falls west of the vortices. This is essentially the Rossby wave propagation mechanism (e.g., Pedlosky 1987, section 3.16; HMR, section 6a). For localized, finite-amplitude disturbances such as the vortices in the present observed case, however, the dispersive behavior over long timescales is highly nonlinear and, thus, far more complex than the instantaneous behavior depicted in Fig. 8b. The final component of the present problem is the advection of the vortices by the background flow, which is eastward (Fig. 8c). In anticipation of the results of the prognostic inversions, consider further the above thought experiment as applied to the observed case. The tendencies induced by each vortex will exhibit combinations of the vortex–vortex and vortex-retrogression mechanisms, yielding geopotential height tendency signatures as shown in Figs. 9a,b. The signature of the background flow is simply downstream advection (Fig. 9c). For a situation such as the present case, where the background-flow signature is dominant, the total geopotential height tendency will possess a similar signature, modified by the vortex contributions (Fig. 9d), such that there are weak (strong) geopotential height rises and falls upstream and downstream (with respect to the background flow) of S1 (S2). With the patterns hypothesized in Fig. 9,
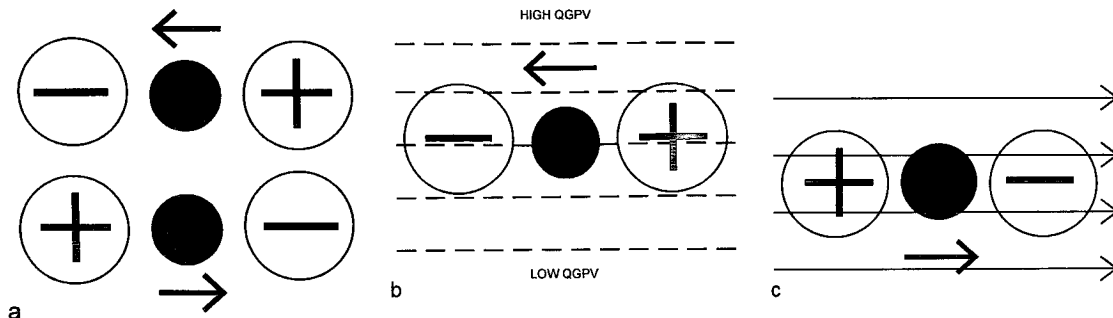
FIG. 8. Schematic illustration of geopotential height tendencies associated with (a) vortex–vortex interactions, (b) vortex retrogression in the presence of a northward-directed background QGPV gradient, and (c) background-flow advection of vortex QGPV. Positive (negative) signs indicate the sense of geopotential height tendencies. The blackened regions denote the location of vortices and heavy arrows show the instantaneous vortex motion. The dashed contours in (b) represent the QGPV associated with the background flow, and the thin arrows in (c) indicate the background geostrophic wind.

we may proceed to interpret the results of the observed case.

At 25/12, the main contribution of the self-induced flow associated with S1 is westward movement at 500 hPa (Fig. 10a). Most of this forcing is due to advection of the surrounding environmental QGPV, since the flow field from S1 is essentially tangent to its own QGPV. The S1-induced flow at S2 is acting to force S2 eastward (Fig. 10a), as surmised from the static-inversion results (Fig. 6b). These respective tendencies are due to the vortex self-propagation mechanism (Fig. 8b) and the vortex–vortex interaction mechanism (Fig. 8a), as discussed above in the idealized thought experiment (Fig. 9a). Geopotential height tendencies associated with S2 indicate that it is forcing S1 westward, while also forcing itself westward by advecting the environmental QGPV distribution (Fig. 10b). These respective tendencies are consistent with those displayed in the simple thought experiment (Fig. 9b).

The third component of the forcing is that due to the background flow. At 25/12, the background flow is acting to force S1 southeastward and S2 east-northeastward (Fig. 10c). As suggested by the static-inversion results (Fig. 7b), the background advections of the vortices dominate the vortex interactions, as in the idealized case (Fig. 9c). The sum of these three fields yields the total QG geopotential height tendency (Fig. 10d); note the qualitative agreement with the idealized case (Fig. 9d). Geopotential height fall centers are focused downstream of S1 and S2 in a larger region of moderate geopotential height falls. At 1000 hPa, the geopotential height tendencies exhibit the gross structure seen at 500 hPa, but the geopotential height falls in the cyclogenesis region are due exclusively to the background flow (Fig. 11). To diagnose further the development of the surface cyclone, the geopotential height tendency induced by the background flow is partitioned into the following four components: background-flow advection of S1 QGPV, background-flow advection of S2 QGPV, background-flow advection of

background-flow QGPV, and background-flow advection of perturbation potential temperature at the upper and lower boundaries. These respective components are evaluated at the grid point of lowest geopotential height corresponding to the 1000-hPa cyclone center at 6-h intervals between 25/12 and 26/06. The results of this evaluation are presented in Table 3, which also contains the geopotential height tendencies at the 1000-hPa cyclone center induced by S1 and S2, respectively. At 25/12, contributions to development due to the background-flow advection of S1, S2, and background-flow QGPV are comparable, whereas the background-flow advection of boundary perturbation potential temperature largely offsets these contributions (Table 3).

With S1 and S2 closer together at 25/18, their interactions at 500 hPa are somewhat more robust (Figs. 12a,b) than at 25/12 (Figs. 10a,b). However, the background flow still dominates, with tendencies reaching -50 to -60 dam $(12 \text{ h})^{-1}$ at 500 hPa (Fig. 12c). The total geopotential height tendency at 25/18 (Fig. 12d) reflects the in- (out-of-) phase relationship between the forcing by S1 on S2 (S2 on S1) and by the background flow on S2 (S1). Here, S1 is forcing geopotential height falls (rises) east (west) of S2, while the opposite is true of the forcing by S2 on S1 (Figs. 12a,b; see also Figs. 9a,b). The vortex-retrogression mechanism opposes the background-flow-induced tendencies at both S1 and S2 (Figs. 12a–c). At 1000 hPa, the background-flow component (Fig. 13c) constitutes nearly all of the total geopotential height falls (Fig. 13d) in the cyclogenesis region. The maximum geopotential height falls are located just northeast of the cyclone centered over Alabama, with falls extending southward in advance of the cold front associated with this cyclone. This region of geopotential height falls also extends westward and southward over Mississippi, in the vicinity of a second cyclone (see HBK, Fig. 11). Compared to 25/12, the partition of the tendency induced by the background flow at 25/18 (Table 3) indicates increased height falls due to background-flow advec-
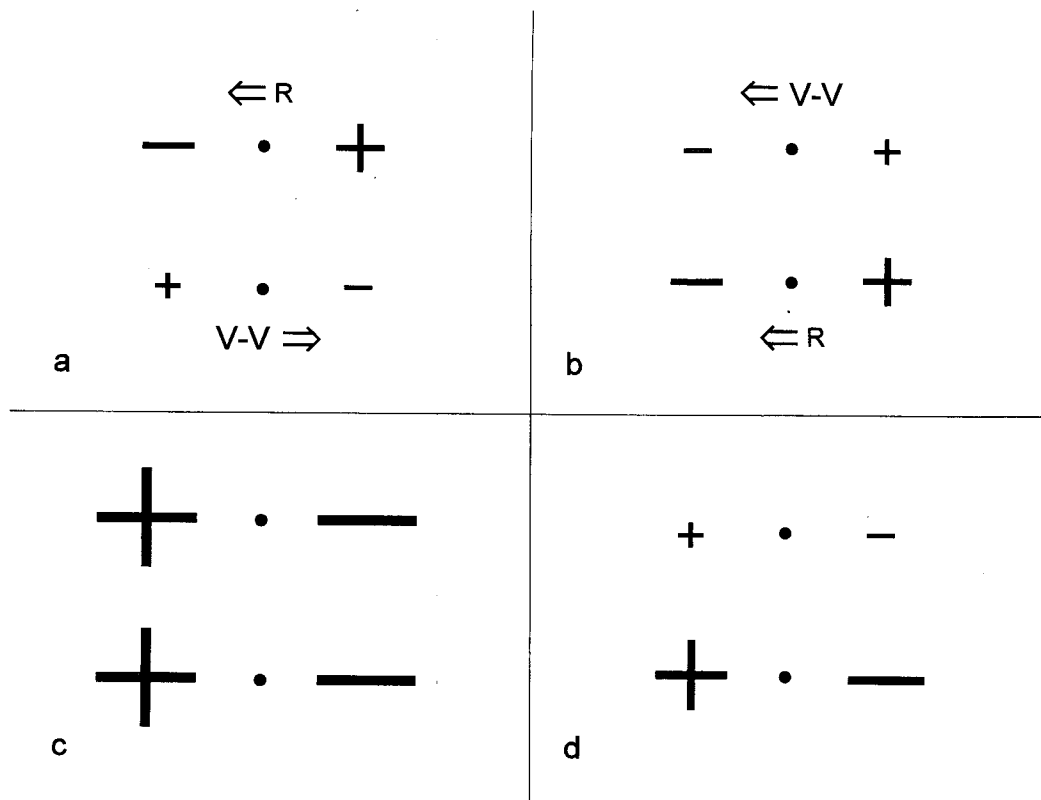
FIG. 9. Schematic illustration of geopotential height tendencies for a hypothetical situation where two cyclonic vortices of equal strength are separated meridionally within a northward-directed background QGPV gradient. The background flow consists of a uniform zonal current, and the geopotential height tendencies induced by the background flow are assumed to be dominant. The geopotential height tendencies induced by the northern vortex are shown in (a), the southern vortex in (b), and the background flow in (c). The net geopotential height tendencies are shown in (d). Using the nomenclature of Fig. 8, the near-vortex tendencies in (a) and (b) are dominated by the vortex-retrogression mechanism (R), and the far-vortex tendencies are dominated by the vortex–vortex mechanism ($V-V$). The sizes of the "+" and "−" symbols are proportional to the geopotential height tendencies ($V-V$, R, and background-flow tendencies are scaled by a ratio of 1:2:4), and the arrows in (a) and (b) indicate instantaneous direction of vortex movement.

tion of S1 and S2 QGPV, reduced height falls due to background-flow advection of background-flow QGPV, and significantly reduced height rises due to background-flow advection of boundary perturbation potential temperature. These respective changes are manifested as a net increase in the magnitude of the diagnosed total geopotential height tendency, consistent with the increase found in the magnitude of the analyzed tendency (Table 3).[2]

. Although the vortex interactions are more robust as S1 and S2 approach each other at 26/00, the background forcing still dominates at 500 hPa (Fig. 14).

[2] The discrepancies between the total and the analyzed geopotential height tendencies in Table 3 are a result of the approximations inherent to the adiabatic, frictionless QG system used to diagnose the former and of the coarse temporal resolution (6 h) of the ECMWF dataset used to evaluate the latter.

The S1 forcing of S2 continues to enhance the effects of the background flow near the developing surface cyclone (Figs. 14a,c), and the vortices still tend to counterpropagate in the absence of other mechanisms (Figs. 14a,b). At 1000 hPa, the background flow is inducing geopotential height falls mainly east of the Appalachian Mountains in the location toward which a cyclone in northern Georgia is moving at this time (Fig. 15c). Large falls also extend northwestward toward southern Ohio in the vicinity of the track of the main cyclone during 26/00–26/06 (Fig. 15c). At the point of lowest 1000-hPa geopotential height, development is due almost exclusively to background-flow advection of S1 and S2 QGPV (Table 3). Although this result might suggest that S1 and S2 are of nearly equal importance in cyclogenesis at 1000 hPa, further consideration of the respective tendencies induced by S1 and S2 (Figs. 15a,b and the third and fourth columns of Table 3) indicates that the vortex-retrogression tendency of S2
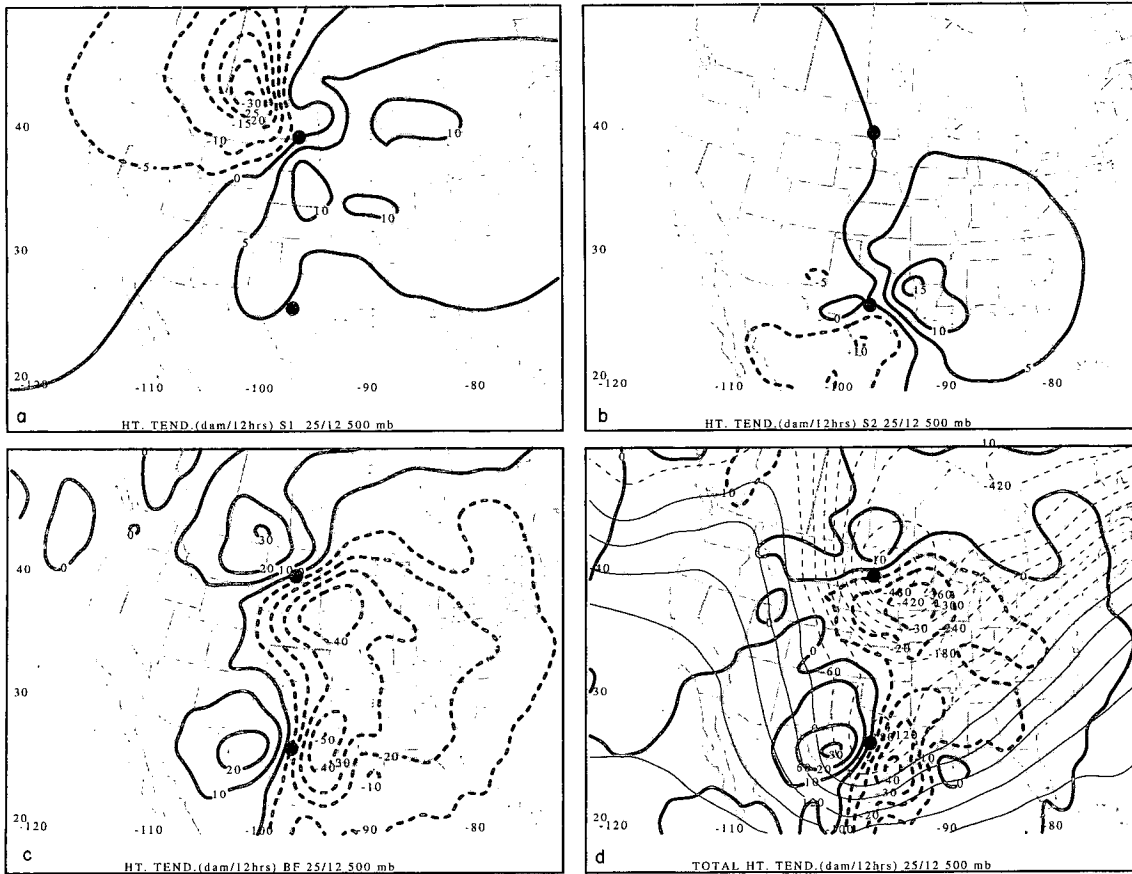
FIG. 10. Prognostic-inversion solutions for 500 hPa at 25/12. The geopotential height tendencies [dam $(12 \text{ h})^{-1}$] induced by the northern vortex (S1) are shown in (a), the southern vortex (S2) in (b), and the background flow in (c). The total QG geopotential height tendencies (sum of panels a, b, and c) are shown in (d), along with the 500-hPa perturbation geopotential height field (m, thin lines). The large dots in each panel indicate the positions of S1 and S2.

significantly offsets the background-flow advection tendency of S2 at the location of the 1000-hPa cyclone center. In contrast, the vortex-retrogression tendency of S1 does not counteract the background-flow advection of S1 to a significant extent at this location. This comparison implies that although S1 is located farther away from the 1000-hPa cyclone center than is S2, the net effect of S1 is more important to the development of the 1000-hPa cyclone than is S2 at this time.

At the time of most rapid surface cyclogenesis (26/06), the vortex interactions at 500 hPa are also greatest, such that considerable overlap occurs between the geopotential height tendencies associated with S1 and S2 (Figs. 16a,b). Even so, background-flow advections remain dominant (Fig. 16c). The horizontal scale contraction of S2 since 25/12 (see Figs. 1d, f and HBK, section 4) probably contributes to the progressively enhanced advections (not shown) and geopotential height tendencies that have occurred in its vicinity at 500 hPa during the past 18 h. At 1000 hPa, geopotential height falls due to the background flow (Fig. 17c) are spread

over a large area from the Great Lakes to the mid-Atlantic region, with the largest values situated over the mid-Atlantic coast in the vicinity of a secondary cyclone (HBK, Fig. 16). The total geopotential height tendency shows an elongated region of falls extending from Michigan to the East Coast (Fig. 17d). The main cyclone tracks to the west of the maximum in 1000 hPa total geopotential height falls. The westward extension of the total geopotential height falls from the mid-Atlantic maximum to the Ohio Valley is due to background-flow advection of S1 (not shown). This mechanism also is the largest contributor to development at the 1000-hPa cyclone center, with lesser contributions from background-flow advection of S2, background-flow QGPV, and boundary perturbation potential temperature (Table 3).

The foregoing prognostic-inversion results further illustrate the interactions described in HBK (section 6) and quantified by the present static-inversion results. In particular, the background flow dominates the evolution of the flow and forces the vortices to-
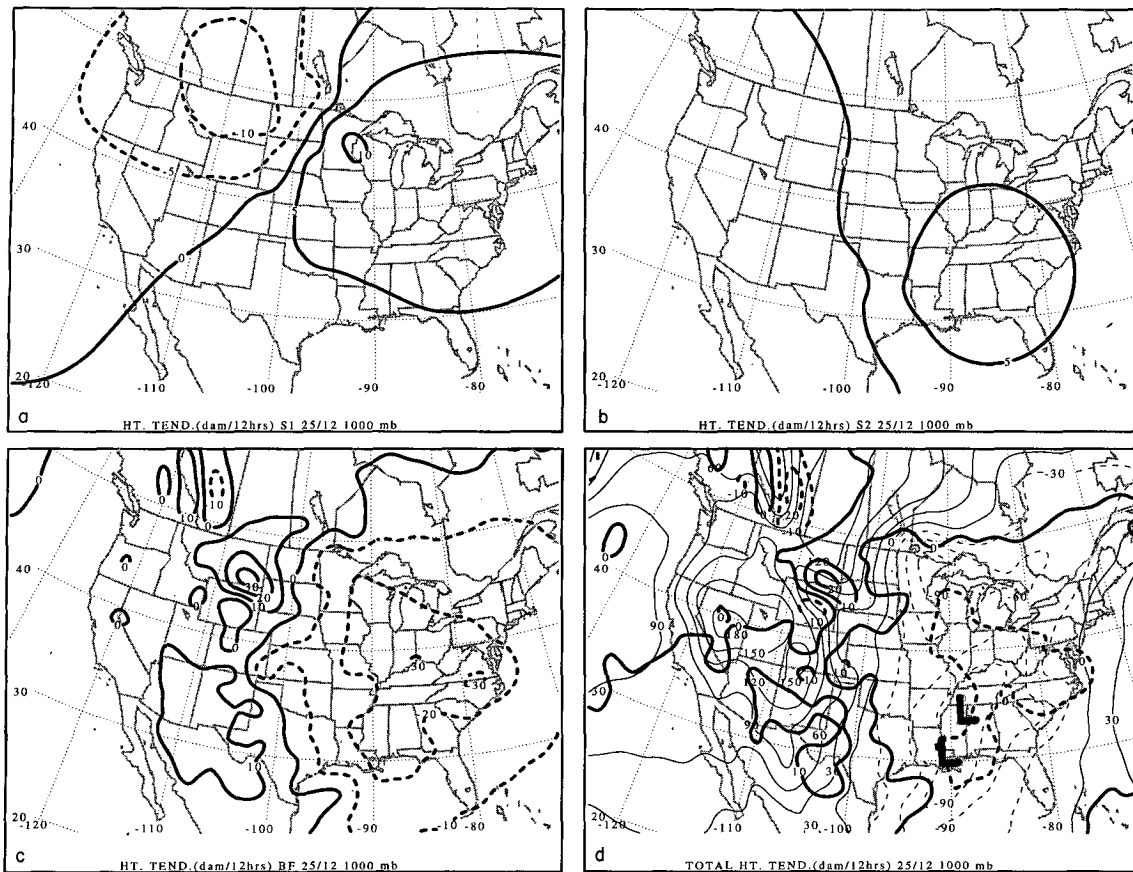
FIG. 11. As in Fig. 10 except for 1000 hPa. The "L" symbols in (d) denote the positions
of surface cyclones, taken from Hakim et al. (1995).

gether. The vortex forcing becomes more robust with time, with S1 forcing of S2 in phase with the background-flow forcing of S2 at 500 hPa in the region of low-level cyclogenesis. At low levels, a significant fraction of the forcing for cyclogenesis is due to background-flow advection of S1 and S2. During rapid cyclogenesis (26/06), the background flow forces geopotential height falls east of the main cy-

clone in the vicinity of the secondary cyclone, which tracks along the coastal front. Based on the partitioned tendency calculations presented here, we conclude that the background-flow advection of S1 is crucial to the rapid development of the surface cyclone. The same mechanism forces the surface cyclone to track to the west of the Appalachian Mountains, as opposed to the coastal-front track favored

TABLE 3. Prognostic-inversion solutions for 1000 hPa at the grid point of minimum perturbation geopotential height corresponding to the 1000-hPa cyclone center for each date/time given in the first column. The second column gives the minimum 1000-hPa perturbation geopotential height (m), the location of which may be determined from Figs. 11d, 13d, 15d, and 17d for the respective times given below. Continuing to the right, the following 1000-hPa geopotential height tendencies [dam $(12 \text{ h})^{-1}$] are shown: S1 advection of total QGPV, S2 advection of total QGPV, background-flow advection of S1 QGPV, background-flow advection of S2 QGPV, background-flow advection of background-flow QGPV, background-flow advection of the lowest- and highest-layer perturbation potential temperature (boundary condition), total, and analyzed (12-h time-centered difference). The contribution of the inhomogeneous Dirichlet condition specified on the vertical boundaries is incorporated into the tendency due to the background-flow advection of background-flow QGPV.

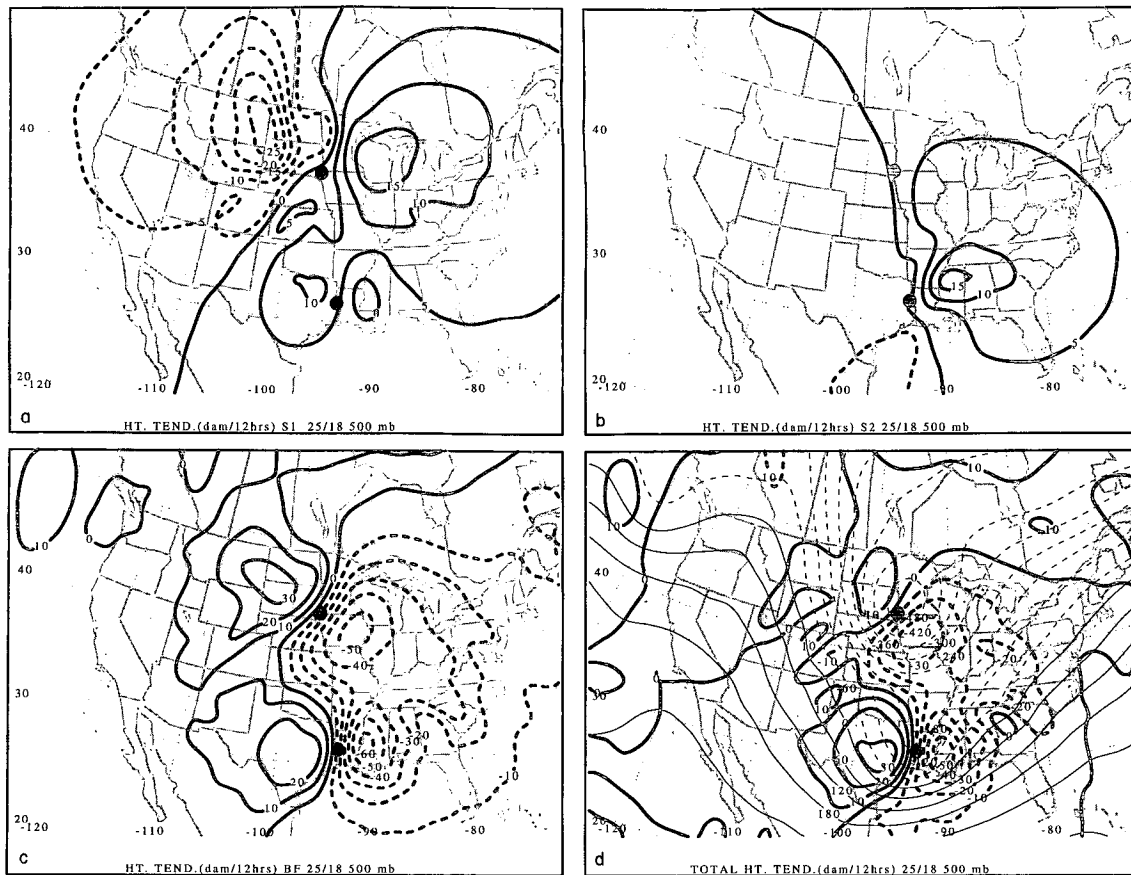| Date/time	z'_{min}	S1	S2	BF-S1	BF-S2	BF-BF	BC	Total	Analyzed
25/12	−103	3.4	5.1	−8.6	−9.6	−9.0	14.4	−4.3	−1.1
25/18	−193	4.8	6.6	−13.4	−12.0	−6.9	1.1	−19.8	−5.7
26/00	−255	3.7	10.7	−15.1	−16.4	1.9	−0.7	−15.9	−8.9
26/06	−386	3.4	8.1	−15.5	−10.0	−7.5	−3.1	−24.6	−11.1

FIG. 12. As in Fig. 10 except for 25/18.

by the weaker secondary cyclone (Fig. 17d). Additional calculations (not shown) indicate that in the absence of S1 the main area of geopotential height falls would have been located east of the Appalachians. This leads to the speculation that the main surface cyclone might have tracked along the mid-Atlantic coast and not have been as intense in the absence of S1.

6. Simple dynamical model and interpretations

QGPV inversion has been used in this work to partition the dynamics attributable to features identified from a synoptic analysis of this case of wave-merger cyclogenesis (HBK). The scenario suggested by the inversion results involves two interacting vortices in an evolving background flow characterized by confluence. Given these three fundamental constituents of the present event, we proceed to explore the characteristics and behavior of a simple model comprising these constituents. To motivate this simple model, we first consider conceptually the behavior of a pair of QG baroclinic vortices on an f plane.

In a QG model atmosphere on an f plane, a pair of baroclinic vortices may be specified initially as localized spheres of cyclonic QGPV ($q_* > 0$). Because these volumes are perfectly symmetric at the initial time, the associated flow fields will be in the form of symmetric vortices with flow speed decreasing radially beyond the edges of the spheres of q_*. Viewed from the pressure surface on which these two vortices are centered, the horizontal shear flow attributed to one of these vortices will act to deform the initially circular q_* field associated with the other vortex. Thus, the velocity field associated with each vortex will evolve in time in response to distortions to its q_* distribution induced by the flow associated with the other vortex. In the observed case, the vortices interact via these mutual advections, changing shape while orbiting each other (Fig. 6). In the presence of a background-flow field that brings the vortices closer together, the interactions become more robust. In the case examined here, although the distribution of q_* associated with each vortex becomes distorted, the perturbation geopotential height field, and hence the geostrophic wind, at locations distant from each vortex (i.e., greater than the e-folding dis-

HT. TEND.(dam/12hrs) S1 25/18 1000 mb

HT. TEND.(dam/12hrs) S2 25/18 1000 mb

HT. TEND.(dam/12hrs) BF 25/18 1000 mb

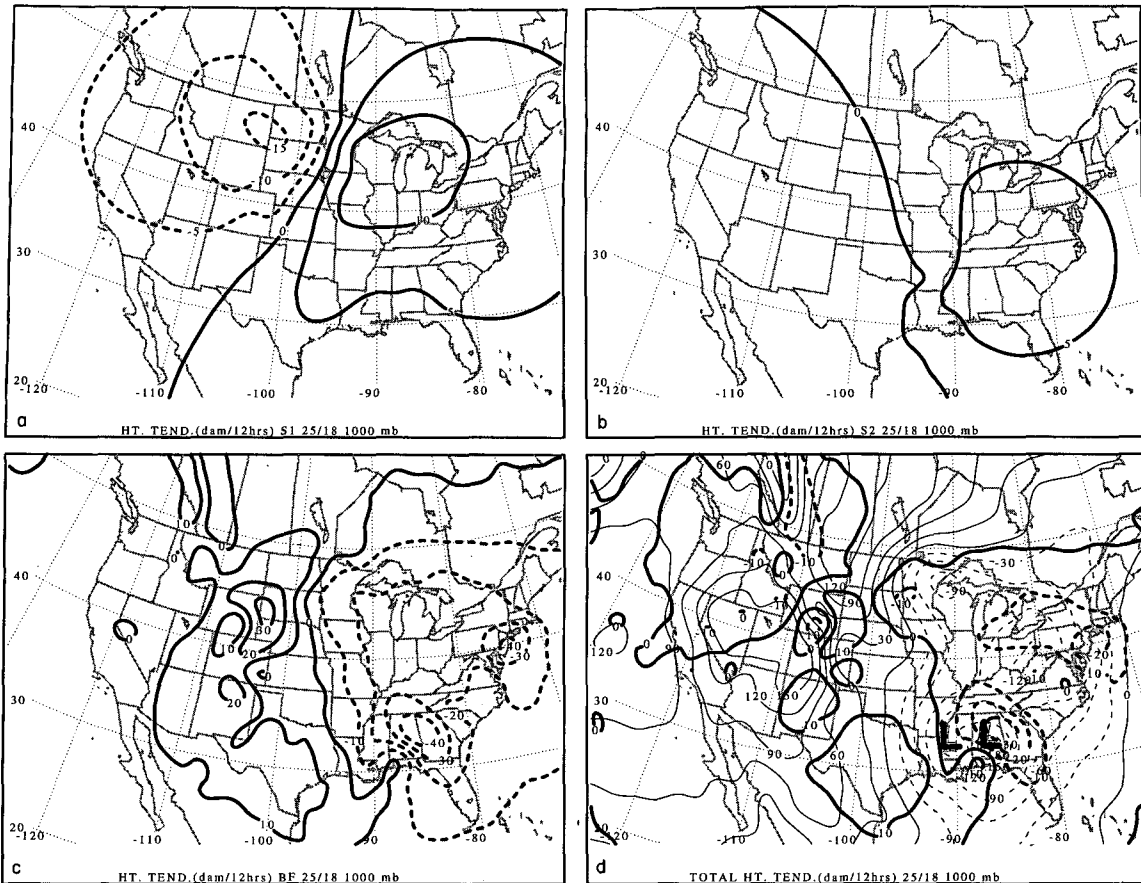TOTAL HT. TEND.(dam/12hrs) 25/18 1000 mb

FIG. 13. As in Fig. 11 except for 25/18.

tance; see Fig. 6) does not deviate appreciably from circular symmetry. This tendency toward circular symmetry apparent in the static-inversion results is due to the smoothing properties of the horizontally isotropic operator (3).

Deformation-induced changes to the wind field attributable to each system can be removed in the limit where the spheres shrink to points (δ functions of q_*). The point elements of q_* still induce vortex flows; however, the resulting solutions will have the important additional property that the velocity field associated with each vortex is conserved for all time. The simplest model that supports the dynamics of these point vortices is the inviscid, nondivergent barotropic vorticity equation on an f plane. Here we need to consider only one level and the QGPV reduces to relative vorticity. The point-vortex representation has a rich history of application in fluid dynamics; for background material the reader is directed to Batchelor (1967, 530–532). To facilitate replicating observed vortex structure and behavior, we specify small-area patches of constant relative vorticity. These patches are referred to as "particles"—although they are not point sources, it is mandated that they cannot be deformed. For a

given circulation, the particle and point vortex wind fields are the same from the edge of the particle to infinity.

The QGPV conservation equation for an inviscid, nondivergent barotropic atmosphere on an f plane reduces to the conservation of relative vorticity:

$$\frac{\partial}{\partial t} \nabla^2 \psi + J(\psi, \nabla^2 \psi) = 0, \tag{15}$$

where

$$\nabla^2 \psi = \zeta \tag{16}$$

is the relative vorticity (hereafter referred to as vorticity) and J is the Jacobian operator. Consider a situation where the only vorticity that exists on an infinite horizontal plane is constant (denoted by ζ_0) and localized on a particle that is circular with radius ϵ. The streamfunction associated with the particle is given by

$$\psi(r) = \begin{cases} \dfrac{\epsilon^2 \zeta_0}{2} \ln\left(\dfrac{r}{\epsilon}\right), & r \geq \epsilon. \quad (17a) \\[4mm] \dfrac{\epsilon^2 \zeta_0}{4}\left[\left(\dfrac{r}{\epsilon}\right)^2 - 1\right], & r \leq \epsilon. \quad (17b) \end{cases}$$
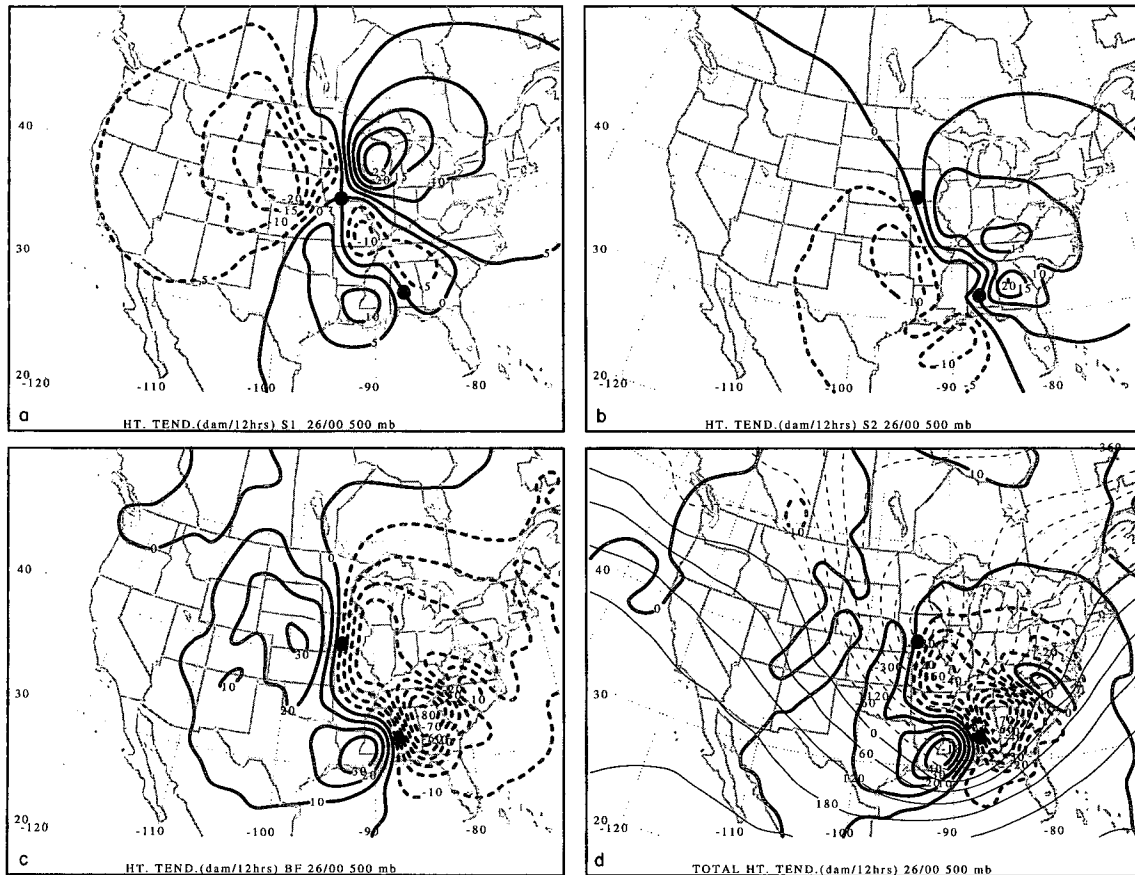
FIG. 14. As in Fig. 10 except for 26/00.

This solution, for which the free parameters are ζ_0 and ϵ, corresponds to a Rankine vortex (e.g., Saffman 1992, p. 22): the azimuthal wind field for this vortex flow [i.e., $V(r) = \partial\psi/\partial r$] increases linearly from zero at the center to a maximum of $\epsilon\zeta_0/2$ at the edge, $r = \epsilon$, and decreases at a rate of r^{-1} to zero again as r approaches infinity. Since a single particle is an exact solution of (15), conservation has been extended beyond the vorticity field to the streamfunction for each particle. This property follows from the assumption that the particle is not deformable. All that is required to solve any flow problem described by (15) are the initial location, size (ϵ), and strength (ζ_0) of each particle, along with the background flow, which uniquely determine the trajectories of the particles constituting the flow system.

Although analytical solutions are possible, even for large numbers of particles provided that certain symmetry requirements are satisfied (Aref et al. 1992), the incorporation of a background-flow field into our model violates these requirements. Consequently, solutions are obtained using numerical integration to determine particle trajectories. Trajectories are found by forward time stepping the position of each particle us-

ing the vector wind at the particle. Solutions to the particle model are found using a nondimensionalized form of the derivation. Dimensionalized values are obtained by the following scaling of nondimensional variables in terms of the free parameters ζ_* and ϵ_*: $\zeta = \zeta_*\tilde{\zeta}$, $\epsilon = \epsilon_*\tilde{\epsilon}$, $\alpha = \alpha_*\tilde{\alpha}$, $V = V_*\tilde{V}$, and $t = t_*\tilde{t}$, where $\alpha_* = \zeta_*$, $V_* = \epsilon_*\zeta_*$, and $t_* = 1/\zeta_*$. Here, dimensional variables are unsubscripted, the subscript asterisk represents the scaling parameter of the nondimensional variables, $\zeta_* = f_0 = 10^{-4}$ s^{-1}, $\epsilon_* = 250$ km, and α is the deformation parameter (see below). Initial conditions are chosen to be representative of those determined from the static inversions at 25/00 and 25/12: two cyclonic vortices displaced a large distance meridionally and a smaller distance zonally (Fig. 6a). The northern system has a radius ϵ of 250 km and a relative vorticity ζ_0 of $4f_0$, yielding a maximum wind speed $2\epsilon f_0$ of 50 m s^{-1} at its edge (cf. with Fig. 5a). The southern system also has a relative vorticity of $4f_0$, with a radius of 187.5 km, which gives a maximum wind speed of 37.5 m s^{-1}. The meridional and zonal separations are 2500 km and 500 km, respectively, with the northern system lying to the east of the southern system. The background flow consists of a hyperbolic deformation field given by ψ_{bf}
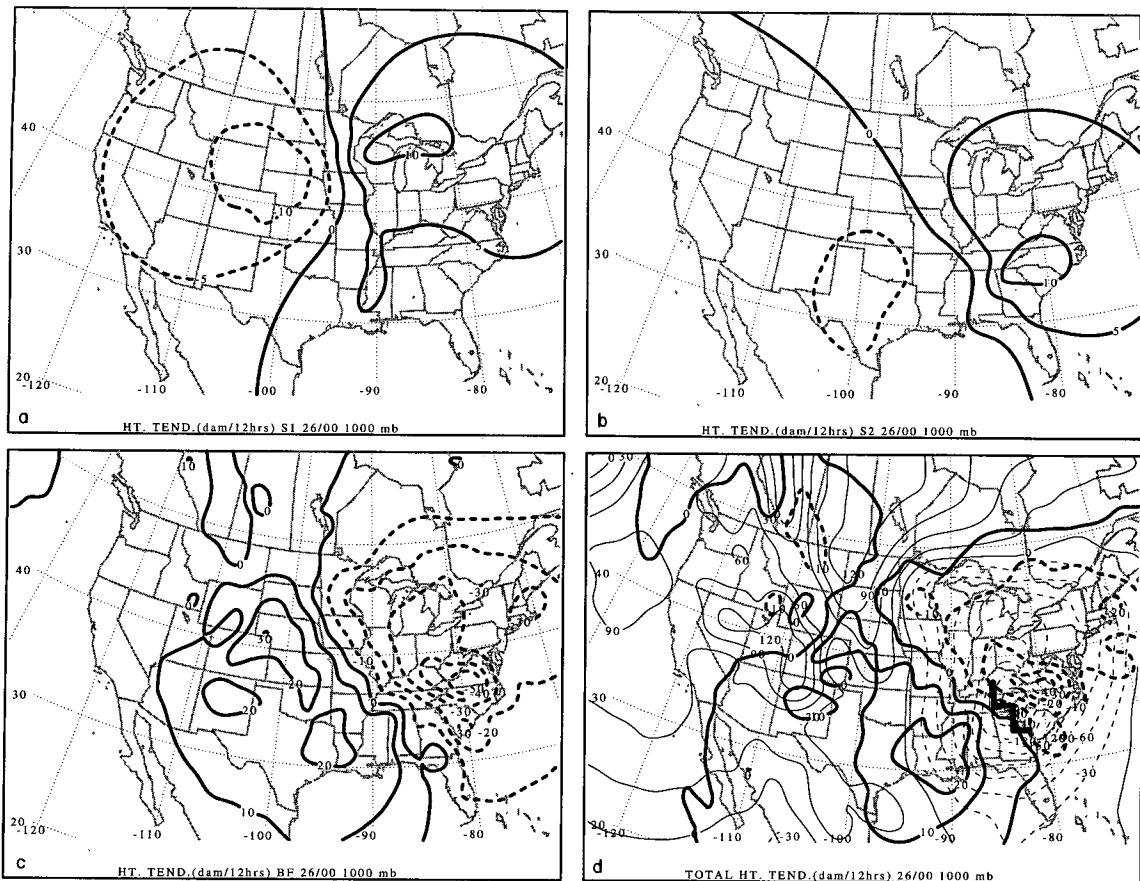
FIG. 15. As in Fig. 11 except for 26/00.

= $-\alpha xy$, which is fixed in time. The parameter α controls the strength of the background flow. A translational flow component could be imposed to simulate the jet stream in which these features are embedded; however, this elaboration is avoided here for the sake of simplicity.

For $\alpha = 2.36 \times 10^{-5}$ s^{-1}, the background-flow wind speed is 30.1 m s^{-1} at the initial positions of the vortices, roughly the analyzed value. At the southern (northern) vortex, the wind speed induced by the northern (southern) vortex is 4.9 (2.8) m s^{-1}; these wind speeds may be compared with values of approximately 2 (1) m s^{-1} determined from the static inversions. The evolution of the vortices in the model exhibits a combination of vortex–vortex and vortex–background-flow advections (Fig. 18). The long-term behavior is a close approach (i.e., "merger") of the two vortices (Fig. 18d), similar to the evolution in the observed case. The dimensional time for Fig. 18d is 38.9 h, which compares with about 36 h for the analogous evolution in the observed case (25/00–26/12). Thus, the timescale of these barotropic simulations is the same order as observed when the initial conditions and the deformation parameter are selected to conform to the observations. The apparent success of this simple

model in replicating some of the observed characteristics of this case of trough merger does not imply that this phenomenon is described completely by barotropic dynamics. For instance, the background-flow field is far more complicated than a simple hyperbolic deformation field, and the change in the orientation of the trough axis in the background flow has not been taken into account (Fig. 7).

When α is increased to 2.60×10^{-5} s^{-1}, a different behavior results (Fig. 19). By $\tilde{t} = 4$ (11.1 h), the evolution is nearly identical to that in the merger simulation (cf. Figs. 18b and 19b). However, in this case the northern system is stripped away before merger can occur (Figs. 19c,d). The reason for this behavior is that the background deformation dominates the vortex flows and leads to a divergence of the vortices in time. The speed of the deformation flow at the initial positions of the particles is 33.1 m s^{-1}, an increase of only 3 m s^{-1} from the merger case. If α is decreased to 1.0 $\times 10^{-5}$ s^{-1}, yet another behavior arises (Fig. 20). In this case, the vortex–vortex interactions dominate the background deformation long enough to result in a divergent behavior that is opposite to that of the previous case (Fig. 19). At $\tilde{t} = 0$, the speed of the defor-
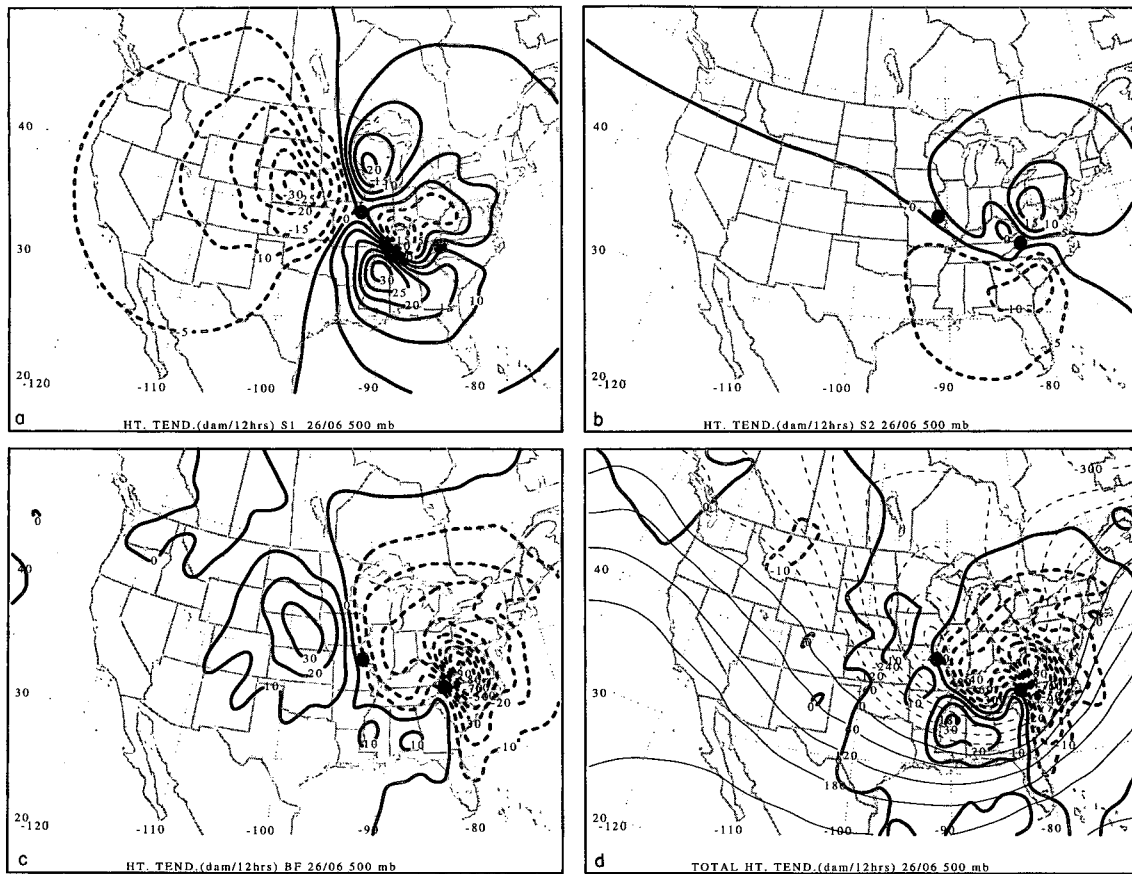
FIG. 16. As in Fig. 10 except for 26/06.

mation wind field at the particles is 12.7 m s^{-1}. Note that the dimensional timescale for this evolution, 55.6 h (Fig. 20d), is considerably longer than in the merger case. However, since this evolution occurs over a reasonable synoptic timescale and for a realistic value of the deformation parameter, this type of evolution should not be considered any less likely than merger.

The results of these particles-in-a-field experiments indicate that for the initial conditions considered here an accurate knowledge of the background deformation is crucial to predicting the subsequent evolution. The implications of the results of the three simulations are clarified by graphing the minimum (i.e., close-approach) distance between the particles during a simulation as a function of α for the initial particle positions, sizes, and strengths used in the simulations shown in Figs. 18–20. The results for 1000 simulations are shown in Fig. 21. For $\alpha = 0$, the minimum separation is the initial separation (10.2 nondimensional units), which remains constant with time. When α is very small, the vortex interactions dominate the flow evolution early, and the vortices do not come very close together. The example shown in Fig. 20 is representative of this evolution. As α increases, the minimum

distance between the vortices becomes smaller. The action of the deformation is to bring them closer together. In addition, the time required to achieve closest approach decreases rapidly with increasing α for relatively small values of α. A minimum in the close-approach time, about 25 h, occurs at smaller values of α than does the minimum in the close-approach distance. Beyond the minimum in close-approach time, increasingly longer times are required to achieve the close-approach distance as a critical value of α ($\alpha_c = 2.41 \times 10^{-5}$ s^{-1}) is attained. At this critical value of α, the vortices achieve their minimum close-approach distance; about 55 h are required to reach this point. Once α increases beyond α_c, a transition to the behavior apparent in the second simulation (Fig. 19) appears. For the given initial conditions, the deformation is strong enough to strip the vortices apart. Additionally, for α increasing beyond α_c, the close-approach time becomes progressively shorter. In all simulations with α smaller (larger) than α_c, the northern vortex lies west (east) of the southern vortex at large time. Figure 21 also illustrates the complex mixture of vortex–vortex and vortex–background-flow interactions that contribute
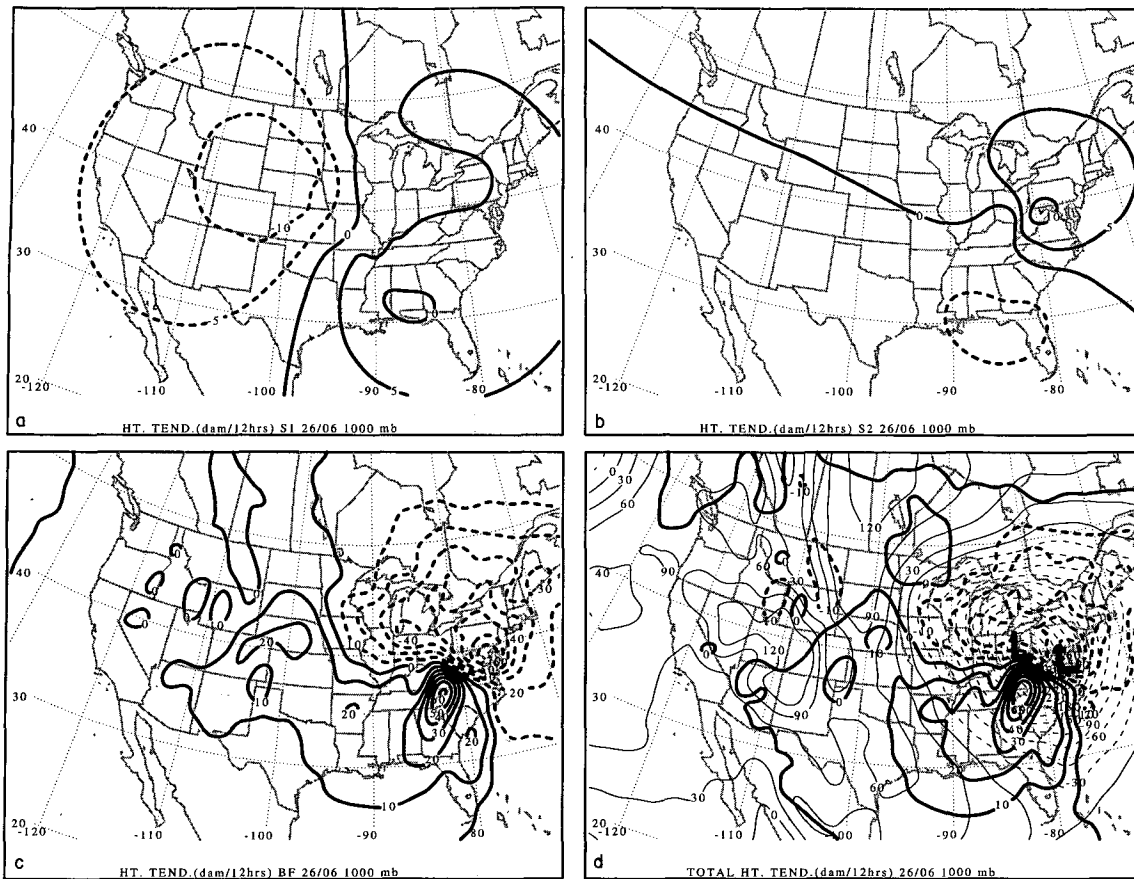
FIG. 17. As in Fig. 11 except for 26/06.

to phasing in this case. Arbitrarily defining merger to be $2.5\epsilon_*$ (625 km) indicates that phasing events lie precariously close to the transition point occurring at α_c.

Although these simulations are highly idealized, they illustrate fundamental behavior of interacting vortices in a deformation flow. There are many implications for forecasting real phasing events of the type studied here. Since errors in observing vortices and background flows are unavoidable, the following question arises: in what situations are these errors significant enough to lead to forecast solutions that exhibit divergent behavior in response to slightly altered initial conditions? The results in Fig. 21 suggest that even if the vortices could be observed perfectly at some initial time, errors in observing the background flow may doom certain forecasts. The results of Fig. 21 imply that if the initial conditions for a forecast lie near the transition point occurring at the critical value of the deformation parameter, α_c, the forecast will be inherently unreliable; that is, the long-term behavior of cases with nearly identical initial conditions may be completely opposite because of the extreme sensitivity of the solutions to small changes in α. The fact that merger events (i.e.,

those exhibiting minimum close approach) in these simulations occur near the transition point suggests a possible explanation of why numerical forecasts of these events may be poor (e.g., Lai and Bosart 1988). Based on our results, determining the actual frequency in which such chaos-type realizations arise in the real atmosphere would make for an interesting predictability study.

7. Discussion and conclusions

Inversion of QGPV is used to elucidate the dynamics of the upper-level precursors and of the background flow for the trough-merger cyclogenesis event that took place over eastern North America on 25–26 January 1978. The QG diagnostic framework is chosen for its relative simplicity and well-established theoretical foundation. Its use is justified in this case by the remarkably high correlation between the QGPV and the Ertel PV. Through inversion of discrete regions of QGPV associated with each of the precursor disturbances, we are able to attribute geostrophic wind and perturbation potential temperature fields to these disturbances. The inversion process allows a piecewise
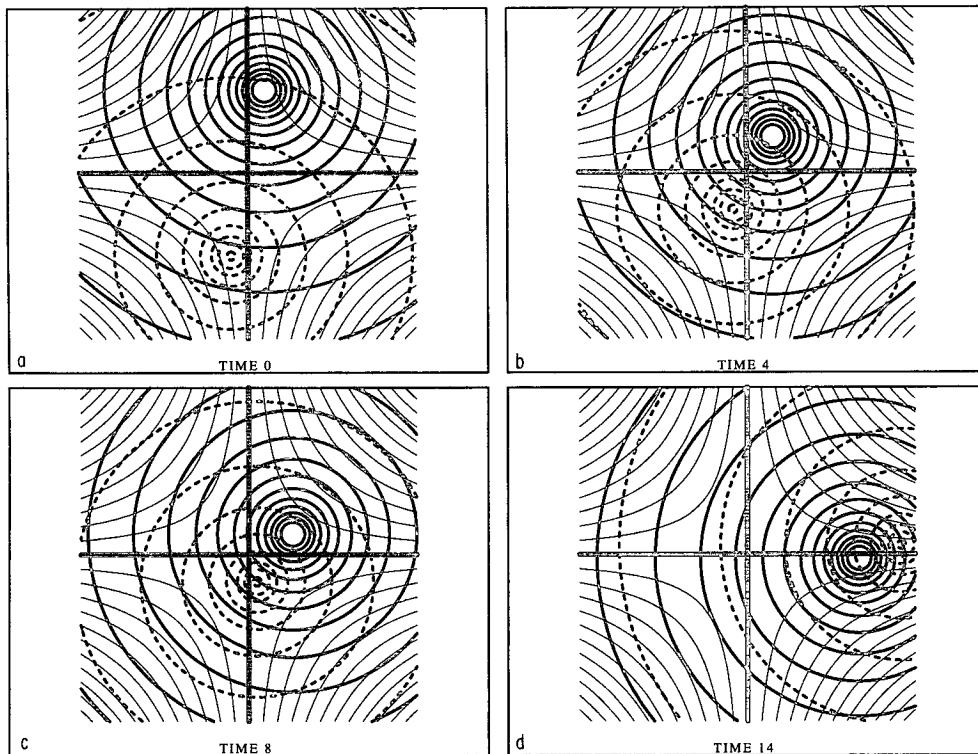
FIG. 18. Streamfunction maps for two cyclonic particles with strength of 4 nondimensional units ($4f_0$ in dimensional units) in a time-independent background flow with deformation parameter $\bar{\alpha} = 0.236$ (2.36×10^{-5} s^{-1}). Additional details concerning the initial specification of the vortex particles (i.e., position and size) are provided in the text in section 6. The streamfunction for the northern system is contoured with thick solid lines every 0.5 nondimensional units, the southern system is contoured with thick dashed lines every 0.5 nondimensional units, and the streamfunction of the deformation flow field is contoured with thin solid lines every 2 nondimensional units. The distance from the origin to the edge of both coordinate axes is 10 nondimensional units, with 1 unit corresponding to 250 km. The time is given in nondimensional units, with 1 unit corresponding to 10^4 s: (a) $t = 0$, (b) $t = 4$, (c) $t = 8$, and (d) $t = 14$.

partition of the flow, and permits use of the QG height tendency equation to quantify the contribution of each flow component to the total time tendency of perturbation geopotential height.

The results of the static QGPV inversions are shown to be sensitive to the choice of boundary conditions. An integral constraint is derived and used to illustrate problems that arise when using Neumann (specification of perturbation potential temperature) and Dirichlet (specification of perturbation geopotential) conditions on horizontal boundaries to attribute the geopotential height field to the QGPV in a localized region. The results of the present case argue for adopting homogeneous Dirichlet conditions on the horizontal boundaries: this alternative yields solutions exhibiting more realistic structure than homogeneous Neumann conditions, and the solutions compare favorably with the free-space Green's function solution, which is independent of boundary conditions.

The upper-level precursor disturbances in the present case possess the structure of baroclinic vortices, while the background flow consists of a synoptic-scale trough. The results of the static and prognostic QGPV inversions indicate a vortex–vortex interaction in confluent large-scale flow. This interaction quantitatively confirms the behavior documented in the synoptic analysis of HBK. The vortices tend to orbit each other, with their interactions strongest after they are brought into close proximity by the confluent background flow. The evolution of the background flow is characterized by a synoptic-scale trough that undergoes a change in orientation from a positive meridional tilt prior to surface cyclogenesis to a negative meridional tilt during surface cyclogenesis. Trough merger in this case is the result of superposition of the flows induced by two vortices in close proximity.

At 500 hPa, piecewise prognostic QGPV inversion, utilizing the partitioned static-inversion flow fields, suggests an interpretation based on the superposition of three fundamental geopotential height tendency signatures associated with two symmetric cyclonic vortices separated meridionally in a northward-directed envi-
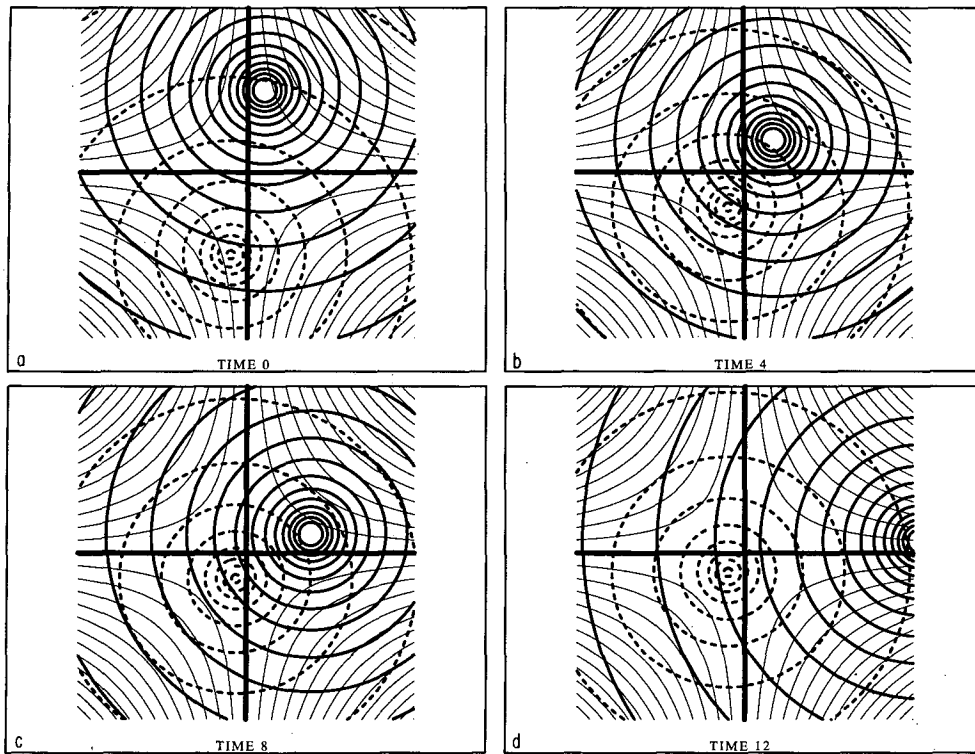
FIG. 19. As in Fig. 18 except $\tilde{\alpha} = 0.26$ $(2.6 \times 10^{-5}$ s$^{-1})$: (a) $\tilde{t} = 0$, (b) $\tilde{t} = 4$, (c) $\tilde{t} = 8$, and (d) $\tilde{t} = 12$.

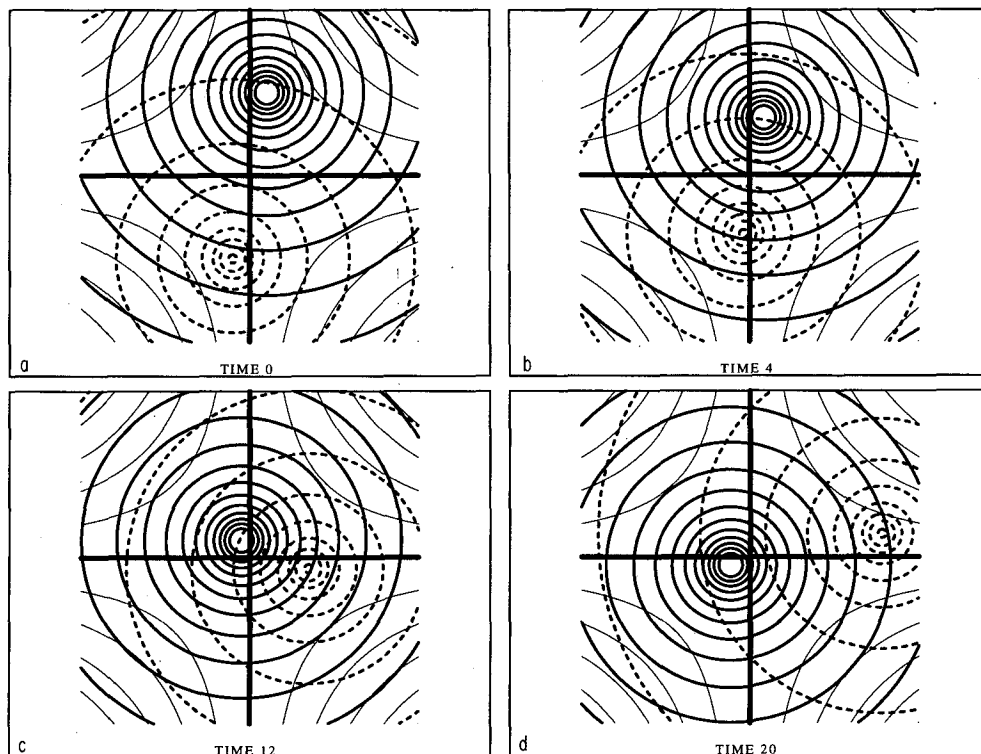FIG. 20. As in Fig. 18 except $\tilde{\alpha} = 0.10$ $(1.0 \times 10^{-5}$ s$^{-1})$: (a) $\tilde{t} = 0$, (b) $\tilde{t} = 4$, (c) $\tilde{t} = 12$, and (d) $\tilde{t} = 20$.

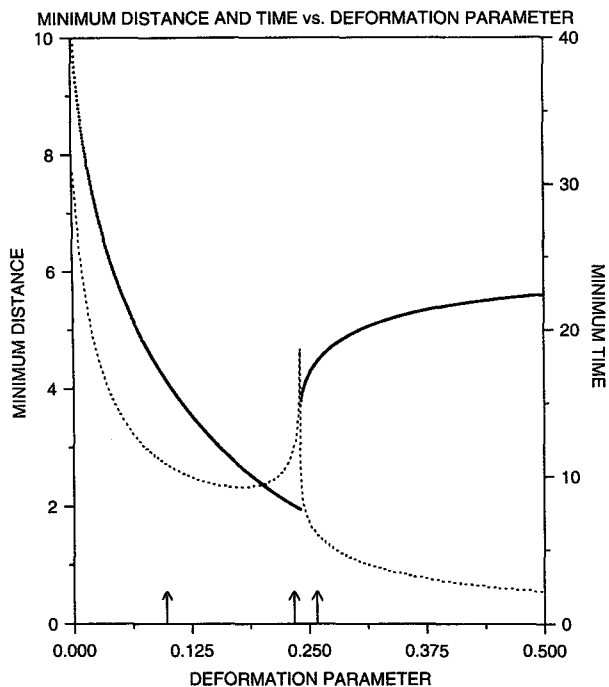MINIMUM DISTANCE AND TIME vs. DEFORMATION PARAMETER

FIG. 21. Graph of minimum nondimensional distance (small dots), and the nondimensional time (short dashes) required to reach this distance, as a function of the nondimensional deformation parameter for 1000 simulations for the specification of the initial particle positions, sizes, and strengths shown in Figs. 18–20. Arrows based on the abscissa indicate values of the nondimensional deformation parameter for the solutions illustrated in Figs. 18–20. See Fig. 18 caption for corresponding dimensional values of unit distance, time, and deformation parameter.

ronmental QGPV gradient. The first signature is a tendency for retrogression of each vortex due to advection of its environmental QGPV field, in the absence of which each vortex would be stationary in isolation, since their flow fields are symmetric to their own QGPV distributions. For the northern vortex, this retrogressive tendency is enhanced by the flow from the southern vortex, whereas for the southern vortex this tendency is opposed by the flow from the northern vortex. These vortex–vortex tendencies increase with time as the vortices approach each other. The third geopotential height tendency signature is that due to the advection of the vortices by the background flow. In this case, the background-flow tendency exceeds both the vortex-retrogression and the vortex–vortex tendencies, and thus controls the motion of the vortices. Geopotential height tendencies at 500 hPa downstream of the southern vortex in the region of low-level cyclogenesis are augmented by the in-phase relationship between the forcing by the background flow and by the northern vortex. The opposite is true at the northern vortex, where the forcing by the southern vortex is acting to oppose the forcing by the background flow.

At 1000 hPa, the prognostic inversions reveal that the incipient cyclogenesis is forced by a combination of the background flow advecting the QGPV of the northern and southern vortices and the QGPV of the background flow. During the period of rapid surface cyclogenesis, background-flow advections of the QGPV of the northern and southern vortices are the primary contributions to deepening the cyclone. Nevertheless, when the geopotential height tendencies due to the advection of total QGPV by the respective flows associated with the northern and southern vortices are taken into account, the net contribution from the northern vortex is in fact more important than that from the southern vortex in forcing geopotential height falls at the point of the 1000-hPa cyclone center. This result is a consequence of the vortex-retrogression tendency of the southern system, which significantly offsets the tendency due to the background-flow advection of this system. This finding of "action at a distance" is not intuitively obvious on the basis of qualitative considerations, because the northern vortex is located farther from the surface cyclone center than is the southern vortex. Of additional interest, advection of the northern vortex by the background flow is found to be the primary agent forcing the main cyclone to track west of the Appalachian Mountains. In the absence of the northern vortex, the main area of geopotential height falls would have been located east of the Appalachians. This leads to the speculation that the main surface cyclone might have tracked along the mid-Atlantic coast and not have been as intense in the absence of the northern vortex.

Based on the results of the QGPV inversions, a simple dynamical model is proposed to expose the fundamental mechanisms documented for this event. As background for this simple model, we consider a conceptual model in which the respective flows from two initially circular baroclinic vortices act to distort the other vortex, such that their subsequent interactions are modified in response to the alteration of their respective QGPV distributions. Although this model allows distortions to occur in the distributions of QGPV associated with each vortex, it is observed that the isotropic properties of the horizontal portion of the QGPV operator cause local asymmetries in the QGPV field to be smoothed out, so that at large distances from the source the perturbation geopotential field tends toward circular symmetry.

Although the symmetric far-field structure of the vortices in the above conceptual model would appear to preclude the possibility of true merger (i.e., irreversible mixing of fluid from the respective vortex cores), it is well established that two like-signed vortices can merge, even in the inviscid case, if the distance between them is less than a critical value. The work of Christiansen and Zabusky (1973) clearly exhibits this behavior in numerical simulations of vortex interactions. The merger process occurs during stages

of vortex interaction when portions of the vortices are distorted into filaments. As these filaments are drawn out from each vortex, the vortex cores approach each other and eventually consolidate into a single elliptical structure (e.g., Zabusky et al. 1979; Overman and Zabusky 1982; Melander et al. 1988). This elliptical structure subsequently relaxes to a circular shape by ejecting vortex filaments from the periphery of the merged vortices. The final result is a single symmetric vortex. Motivation for understanding the merger phenomenon derives from the observation that vortex merger (and fracture) is a fundamental property of geostrophic turbulence (e.g., McWilliams and Chow 1984).

The merger condition for two barotropic vortices of equal strength is that they be separated initially by a distance of less than about 3.2 vortex-core radii (Melander et al. 1988); this value may differ for baroclinic vortices depending on the Rossby radius of deformation (Hopfinger and van Heijst 1993). Using the barotropic criterion for the case studied here, the critical separation distance is roughly 800 km, based on the radius of the northern vortex. Observations show that the closest approach of the vortices is on the order of 900 km at 26/06. Given the short time period over which the vortices are at this separation, it is not surprising that true merger does not occur. The type of merger in the present case is characterized by the superposition of the flows induced by two vortices being driven together by a confluent background flow, which occurs over a short timescale (i.e., about 0.5 orbits) relative to several orbital periods of the vortices. The general problem of vortices in a shearing flow has been treated extensively by Marcus (1990), where merger of two barotropic vortices driven by environmental shear is demonstrated.

Given the observed properties of this cyclogenesis event, use of a model that eliminates the effects of distortion of vortex QGPV is proposed. In its simplest form, the model applies to an inviscid, nondivergent barotropic atmosphere on an f plane and involves specifying rigid, small-area patches (i.e., particles) of relative vorticity. The resulting streamfunction describes an azimuthal wind field exterior to the particle, with the flow speed at a given radius depending on the magnitude of the relative vorticity characterizing the strength of the vortex and on the vortex size. Individual vortex particles have the attractive property of being exact solutions to the nonlinear governing equation for relative vorticity conservation, as well as extending conservation beyond the relative vorticity of a particle to its streamfunction. Conservation of particle streamfunction reduces solution of the model to determining particle trajectories, which depend on the relative positions, sizes, and strengths of each particle in the system, as well as on the background flow. The particle model provides a framework for studying the essence of the behavior of this cyclogenesis event in its simplest con-

text. Two vortex particles, specified by initial conditions representative of observations, are placed within a hyperbolic deformation field, yielding behavior that is encouragingly realistic. A mixture of vortex–vortex and vortex–background-flow interactions results in a close approach of the particles—a merger event. Situations in which the deformation is stronger than a certain critical value yield diverging vortices, as do situations with weaker deformation. The set of solutions corresponding to merger occurs over a narrow range of the deformation parameter for a given set of initial conditions describing vortex position, size, and strength.

The vortex-particle simulations raise several operational forecasting issues. Since the trajectories of the vortices depend upon both the vortex and the background flows, it may be asked exactly how well the initial conditions must be known to prevent large error growth in short-term forecasts. Experiments are conducted where the initial conditions are kept identical, but the strength of the background deformation is allowed to vary. The results exhibit a transition point within the range of values of the deformation parameter that leads to closest approach (i.e., vortex merger). This property of the solutions suggests that observed flow situations involving vortices within a background flow may be very sensitive to subtle errors in the magnitude of the deformation when this magnitude approaches a critical value. Consequently, such situations may yield subsequent behavior that from a practical point of view is completely unpredictable. It would be extremely useful for operational forecasting if these situations could be identified a priori. Of equal importance would be identifying situations in which the subsequent behavior is relatively insensitive to errors in observing the vortices or the background flow. A significant hurdle in this endeavor involves establishing the uncertainty in the nonlinear evolution of the background flow itself, an effect neglected in the particle simulations.

To the extent that the vortex-particle model is applicable to the cyclogenesis event of 25–26 January 1978, it is possible that the large-scale flow was *not* near a critical value in the magnitude of the deformation. Thus, we may speculate that errors in observing this flow did not strongly affect the National Meteorological Center's operational model during January 1978, the Limited-Area Fine-Mesh Model, which was successful in forecasting this extreme event (Salmon and Smith 1980). A similar scenario may have occurred in the "storm of the century" of 12–14 March 1993 over eastern North America. This trough-phasing cyclogenesis event was captured by operational models six days in advance, with little vacillation in the forecast approaching the time of surface cyclogenesis (e.g., Caplan 1995; Uccellini et al. 1995). These considerations, along with an example of problems that operational numerical models exhibit in forecasting trough-phasing cyclogenesis given by Lai and Bosart (1988), suggest

the need for a comprehensive study of model performance in forecasting this phenomenon.

REFERENCES

Anthes, R. A., and D. Keyser, 1979: Tests of a fine-mesh model over Europe and the United States. *Mon. Wea. Rev.,* **107,** 963–984.

Aref, H., N. Rott, and H. Thomann, 1992: Gröbli's solution of the three-vortex problem. *Annu. Rev. Fluid Mech.,* **24,** 1–20.

Batchelor, G. K., 1967: *An Introduction to Fluid Dynamics.* Cambridge University Press, 615 pp.

Bishop, C. H., and A. J. Thorpe, 1994: Potential vorticity and the electrostatics analogy: Quasi-geostrophic theory. *Quart. J. Roy. Meteor. Soc.,* **120,** 713–731.

Black, R. X., and R. M. Dole, 1993: The dynamics of large-scale cyclogenesis over the North Pacific Ocean. *J. Atmos. Sci.,* **50,** 421–442.

Bretherton, F. P., 1966: Critical layer instability in baroclinic flows. *Quart. J. Roy. Meteor. Soc.,* **92,** 325–334.

Burrows, W. R., R. A. Treidl, and R. G. Lawford, 1979: The southern Ontario blizzard of January 26 and 27, 1978. *Atmos.–Ocean,* **17,** 306–320.

Caplan, P. M., 1995: The 12–14 March 1993 Superstorm: Performance of the NMC global medium-range model. *Bull. Amer. Meteor. Soc.,* **76,** 201–212.

Christiansen, J. P., and N. J. Zabusky, 1973: Instability, coalescence and fission of finite-area vortex structures. *J. Fluid Mech.,* **61,** 219–243.

Davies, H. C., and C. H. Bishop, 1994: Eady edge waves and rapid development. *J. Atmos. Sci.,* **51,** 1930–1946.

Davis, C. A., 1992a: A potential-vorticity diagnosis of the importance of initial structure and condensational heating in observed extratropical cyclogenesis. *Mon. Wea. Rev.,* **120,** 2409–2428.

——, 1992b: Piecewise potential vorticity inversion. *J. Atmos. Sci.,* **49,** 1397–1411.

——, and K. A. Emanuel, 1991: Potential vorticity diagnostics of cyclogenesis. *Mon. Wea. Rev.,* **119,** 1929–1953.

Eady, E. T., 1949: Long waves and cyclone waves. *Tellus,* **1,** 33–52.

Farrell, B., 1984: Modal and non-modal baroclinic waves. *J. Atmos. Sci.,* **41,** 668–673.

——, 1985: Transient growth of damped baroclinic waves. *J. Atmos. Sci.,* **42,** 2718–2727.

——, 1989: Optimal excitation of baroclinic waves. *J. Atmos. Sci.,* **46,** 1193–1206.

Gaza, R. S., and L. F. Bosart, 1990: Trough-merger characteristics over North America. *Wea. Forecasting,* **5,** 314–331.

Green, J. S. A., 1987: Comments on "On the use and significance of isentropic potential vorticity maps." *Quart. J. Roy. Meteor. Soc.,* **113,** 401–402.

Hakim, G. J., L. F. Bosart, and D. Keyser, 1995: The Ohio Valley wave-merger cyclogenesis event of 25–26 January 1978. Part I: Multiscale case study. *Mon. Wea. Rev.,* **123,** 2663–2692.

Hollingsworth, A., D. B. Shaw, P. Lönnberg, L. Illari, K. Arpe, and A. J. Simmons, 1986: Monitoring of observation and analysis quality by a data assimilation system. *Mon. Wea. Rev.,* **114,** 861–879.

Holopainen, E., and J. Kaurola, 1991: Decomposing the atmospheric flow using potential vorticity framework. *J. Atmos. Sci.,* **48,** 2614–2625.

Hopfinger, E. J., and G. J. F. van Heijst, 1993: Vortices in rotating fluids. *Annu. Rev. Fluid Mech.,* **25,** 241–289.

Hoskins, B. J., M. E. McIntyre, and A. W. Robertson, 1985: On the use and significance of isentropic potential vorticity maps. *Quart. J. Roy. Meteor. Soc.,* **111,** 877–946.

Lai, C.-C., and L. F. Bosart, 1988: A case study of trough merger in split westerly flow. *Mon. Wea. Rev.,* **116,** 1838–1856.

Marcus, P. S., 1990: Vortex dynamics in a shearing flow. *J. Fluid Mech.,* **215,** 393–430.

McWilliams, J. C., and P. R. Gent, 1980: Intermediate models of planetary circulations in the atmosphere and ocean. *J. Atmos. Sci.,* **37,** 1657–1678.

——, and J. H. S. Chow, 1984: The emergence of isolated coherent vortices in turbulent flow. *J. Fluid Mech.,* **146,** 21–43.

Melander, M. V., N. J. Zabusky, and J. C. McWilliams, 1988: Symmetric vortex merger in two dimensions: Causes and conditions. *J. Fluid Mech.,* **195,** 303–340.

Overman, E. A., and N. J. Zabusky, 1982: Evolution and merger of isolated vortex structures. *Phys. Fluids,* **25,** 1297–1305.

Pedlosky, J., 1987: *Geophysical Fluid Dynamics.* 2d ed. Springer-Verlag, 710 pp.

Robinson, W. A., 1988: Analysis of LIMS data by potential vorticity inversion. *J. Atmos. Sci.,* **45,** 2319–2342.

Rotunno, R., and M. Fantini, 1989: Petterssen's "type B" cyclogenesis in terms of discrete, neutral Eady modes. *J. Atmos. Sci.,* **46,** 3599–3604.

Saffman, P. G., 1992: *Vortex Dynamics.* Cambridge University Press, 311 pp.

Salmon, E. M., and P. J. Smith, 1980: A synoptic analysis of the 25–26 January 1978 blizzard cyclone in the central United States. *Bull. Amer. Meteor. Soc.,* **61,** 453–460.

Thorpe, A. J., 1986: Synoptic scale disturbances with circular symmetry. *Mon. Wea. Rev.,* **114,** 1384–1389.

Uccellini, L. W., P. J. Kocin, R. S. Schneider, P. M. Stokols, and R. A. Dorr, 1995: Forecasting the 12–14 March 1993 superstorm. *Bull. Amer. Meteor. Soc.,* **76,** 183–199.

Whitaker, J. S., and A. Barcilon, 1992: Type B cyclogenesis in a zonally varying flow. *J. Atmos. Sci.,* **49,** 1877–1892.

Zabusky, N. J., M. H. Hughes, and K. V. Roberts, 1979: Contour dynamics for the Euler equations in two dimensions. *J. Comput. Phys.,* **30,** 96–106.